

**High- $p_T$  charged hadron suppression in Au+Au collisions at  $\sqrt{s_{NN}}=200$  GeV**

S. S. Adler,<sup>5</sup> S. Afanasiev,<sup>17</sup> C. Aidala,<sup>5</sup> N. N. Ajitanand,<sup>43</sup> Y. Akiba,<sup>20,38</sup> J. Alexander,<sup>43</sup> R. Amirkhan,<sup>12</sup> L. Aphecetche,<sup>45</sup> S. H. Aronson,<sup>5</sup> R. Averbeck,<sup>44</sup> T. C. Awes,<sup>35</sup> R. Azmoun,<sup>44</sup> V. Babintsev,<sup>15</sup> A. Baldisseri,<sup>10</sup> K. N. Barish,<sup>6</sup> P. D. Barnes,<sup>27</sup> B. Bassalleck,<sup>33</sup> S. Bathe,<sup>30</sup> S. Batsouli,<sup>9</sup> V. Baublis,<sup>37</sup> A. Bazilevsky,<sup>39,15</sup> S. Belikov,<sup>16,15</sup> Y. Berdnikov,<sup>40</sup> S. Bhagavatula,<sup>16</sup> J. G. Boissevain,<sup>27</sup> H. Borel,<sup>10</sup> S. Borenstein,<sup>25</sup> M. L. Brooks,<sup>27</sup> D. S. Brown,<sup>34</sup> N. Bruner,<sup>33</sup> D. Bucher,<sup>30</sup> H. Buesching,<sup>30</sup> V. Bumazhnov,<sup>15</sup> G. Bunce,<sup>5,39</sup> J. M. Burward-Hoy,<sup>26,44</sup> S. Butsyk,<sup>44</sup> X. Camard,<sup>45</sup> J.-S. Chai,<sup>18</sup> P. Chand,<sup>4</sup> W. C. Chang,<sup>2</sup> S. Chernichenko,<sup>15</sup> C. Y. Chi,<sup>9</sup> J. Chiba,<sup>20</sup> M. Chiu,<sup>9</sup> I. J. Choi,<sup>52</sup> J. Choi,<sup>19</sup> R. K. Choudhury,<sup>4</sup> T. Chujo,<sup>5</sup> V. Cianciolo,<sup>35</sup> Y. Cobigo,<sup>10</sup> B. A. Cole,<sup>9</sup> P. Constantin,<sup>16</sup> D. G. d'Enterria,<sup>43</sup> G. David,<sup>5</sup> H. Delagrange,<sup>45</sup> A. Denisov,<sup>15</sup> A. Deshpande,<sup>39</sup> E. J. Desmond,<sup>5</sup> O. Dietzsch,<sup>41</sup> O. Drapier,<sup>25</sup> A. Drees,<sup>44</sup> R. du Rietz,<sup>29</sup> A. Durum,<sup>15</sup> D. Dutta,<sup>4</sup> Y. V. Efremenko,<sup>35</sup> K. El Chenawi,<sup>49</sup> A. Enokizono,<sup>14</sup> H. En'yo,<sup>38,39</sup> S. Esumi,<sup>48</sup> L. Ewell,<sup>5</sup> D. E. Fields,<sup>33,39</sup> F. Fleuret,<sup>25</sup> S. L. Fokin,<sup>30</sup> B. D. Fox,<sup>39</sup> Z. Fraenkel,<sup>51</sup> J. E. Frantz,<sup>9</sup> A. Franz,<sup>5</sup> A. D. Frawley,<sup>12</sup> S.-Y. Fung,<sup>6</sup> S. Garpman,<sup>29,\*</sup> T. K. Ghosh,<sup>49</sup> A. Glenn,<sup>46</sup> G. Gogiberidze,<sup>46</sup> M. Gonin,<sup>25</sup> J. Gosset,<sup>10</sup> Y. Goto,<sup>39</sup> R. Granier de Cassagnac,<sup>25</sup> N. Grau,<sup>16</sup> S. V. Greene,<sup>49</sup> M. Grosse Perdekamp,<sup>39</sup> W. Guryn,<sup>5</sup> H.-Å. Gustafsson,<sup>29</sup> T. Hachiya,<sup>14</sup> J. S. Haggerty,<sup>5</sup> H. Hamagaki,<sup>8</sup> A. G. Hansen,<sup>27</sup> E. P. Hartouni,<sup>26</sup> M. Harvey,<sup>5</sup> R. Hayano,<sup>8</sup> X. He,<sup>13</sup> M. Heffner,<sup>26</sup> T. K. Hemmick,<sup>44</sup> J. M. Heuser,<sup>44</sup> M. Hibino,<sup>50</sup> J. C. Hill,<sup>16</sup> W. Holzmann,<sup>43</sup> K. Homma,<sup>14</sup> B. Hong,<sup>22</sup> A. Hoover,<sup>34</sup> T. Ichihara,<sup>38,39</sup> V. V. Ikonnikov,<sup>23</sup> K. Imai,<sup>24,38</sup> D. Isenhower,<sup>1</sup> M. Ishihara,<sup>38</sup> M. Issah,<sup>43</sup> A. Isupov,<sup>17</sup> B. V. Jacak,<sup>44</sup> W. Y. Jang,<sup>22</sup> Y. Jeong,<sup>19</sup> J. Jia,<sup>44</sup> O. Jinnouchi,<sup>38</sup> B. M. Johnson,<sup>5</sup> S. C. Johnson,<sup>26</sup> K. S. Joo,<sup>31</sup> D. Jouan,<sup>36</sup> S. Kametani,<sup>8,50</sup> N. Kamihara,<sup>47,38</sup> J. H. Kang,<sup>52</sup> S. S. Kapoor,<sup>4</sup> K. Katou,<sup>50</sup> S. Kelly,<sup>9</sup> B. Khachaturov,<sup>51</sup> A. Khanzadeev,<sup>37</sup> J. Kikuchi,<sup>50</sup> D. H. Kim,<sup>31</sup> D. J. Kim,<sup>52</sup> D. W. Kim,<sup>19</sup> E. Kim,<sup>42</sup> G.-B. Kim,<sup>25</sup> H. J. Kim,<sup>52</sup> E. Kistenev,<sup>5</sup> A. Kiyomichi,<sup>48</sup> K. Kiyoyama,<sup>32</sup> C. Klein-Boesing,<sup>30</sup> H. Kobayashi,<sup>38,39</sup> L. Kochenda,<sup>37</sup> V. Kochetkov,<sup>15</sup> D. Koehler,<sup>33</sup> T. Kohama,<sup>14</sup> M. Kopytine,<sup>44</sup> D. Kotchetkov,<sup>6</sup> A. Kozlov,<sup>51</sup> P. J. Kroon,<sup>5</sup> C. H. Kuberg,<sup>1,27</sup> K. Kurita,<sup>39</sup> Y. Kuroki,<sup>48</sup> M. J. Kweon,<sup>22</sup> Y. Kwon,<sup>52</sup> G. S. Kyle,<sup>34</sup> R. Lacey,<sup>43</sup> V. Ladygin,<sup>17</sup> J. G. Lajoie,<sup>16</sup> A. Lebedev,<sup>16,23</sup> S. Leckey,<sup>44</sup> D. M. Lee,<sup>27</sup> S. Lee,<sup>19</sup> M. J. Leitch,<sup>27</sup> X. H. Li,<sup>6</sup> H. Lim,<sup>42</sup> A. Litvinenko,<sup>17</sup> M. X. Liu,<sup>27</sup> Y. Liu,<sup>36</sup> C. F. Maguire,<sup>49</sup> Y. I. Makdisi,<sup>5</sup> A. Malakhov,<sup>17</sup> V. I. Manko,<sup>23</sup> Y. Mao,<sup>7,38</sup> G. Martinez,<sup>45</sup> M. D. Marx,<sup>44</sup> H. Masui,<sup>48</sup> F. Matathias,<sup>44</sup> T. Matsumoto,<sup>8,50</sup> P. L. McGaughey,<sup>27</sup> E. Melnikov,<sup>15</sup> F. Messer,<sup>44</sup> Y. Miake,<sup>48</sup> J. Milan,<sup>43</sup> T. E. Miller,<sup>49</sup> A. Milov,<sup>44,51</sup> S. Mioduszewski,<sup>5</sup> R. E. Mischke,<sup>27</sup> G. C. Mishra,<sup>13</sup> J. T. Mitchell,<sup>5</sup> A. K. Mohanty,<sup>4</sup> D. P. Morrison,<sup>5</sup> J. M. Moss,<sup>27</sup> F. Mühlbacher,<sup>44</sup> D. Mukhopadhyay,<sup>51</sup> M. Muniruzzaman,<sup>6</sup> J. Murata,<sup>38,39</sup> S. Nagamiya,<sup>20</sup> J. L. Nagle,<sup>9</sup> T. Nakamura,<sup>14</sup> B. K. Nandi,<sup>6</sup> M. Nara,<sup>48</sup> J. Newby,<sup>46</sup> P. Nilsson,<sup>29</sup> A. S. Nyanin,<sup>23</sup> J. Nystrand,<sup>29</sup> E. O'Brien,<sup>5</sup> C. A. Ogilvie,<sup>16</sup> H. Ohnishi,<sup>5,38</sup> I. D. Ojha,<sup>49,3</sup> K. Okada,<sup>38</sup> M. Ono,<sup>48</sup> V. Onuchin,<sup>15</sup> A. Oskarsson,<sup>29</sup> I. Otterlund,<sup>29</sup> K. Oyama,<sup>8</sup> K. Ozawa,<sup>8</sup> D. Pal,<sup>51</sup> A. P. T. Palounek,<sup>27</sup> V. S. Pantuev,<sup>44</sup> V. Papavassiliou,<sup>34</sup> J. Park,<sup>42</sup> A. Parmar,<sup>33</sup> S. F. Pate,<sup>34</sup> T. Peitzmann,<sup>30</sup> J.-C. Peng,<sup>27</sup> V. Peresedov,<sup>17</sup> C. Pinkenburg,<sup>5</sup> R. P. Pisani,<sup>5</sup> F. Plasil,<sup>35</sup> M. L. Purschke,<sup>5</sup> A. K. Purwar,<sup>44</sup> J. Rak,<sup>16</sup> I. Ravinovich,<sup>51</sup> K. F. Read,<sup>35,46</sup> M. Reuter,<sup>44</sup> K. Reygers,<sup>30</sup> V. Riabov,<sup>37,40</sup> Y. Riabov,<sup>37</sup> G. Roche,<sup>28</sup> A. Romana,<sup>25</sup> M. Rosati,<sup>16</sup> P. Rosnet,<sup>28</sup> S. S. Ryu,<sup>52</sup> M. E. Sadler,<sup>1</sup> N. Saito,<sup>38,39</sup> T. Sakaguchi,<sup>8,50</sup> M. Sakai,<sup>32</sup> S. Sakai,<sup>48</sup> V. Samsonov,<sup>37</sup> L. Sanfratello,<sup>33</sup> R. Santo,<sup>30</sup> H. D. Sato,<sup>24,38</sup> S. Sato,<sup>5,48</sup> S. Sawada,<sup>20</sup> Y. Schutz,<sup>45</sup> V. Semenov,<sup>15</sup> R. Seto,<sup>6</sup> M. R. Shaw,<sup>1,27</sup> T. K. Shea,<sup>5</sup> T.-A. Shibata,<sup>47,38</sup> K. Shigaki,<sup>14,20</sup> T. Shiina,<sup>27</sup> C. L. Silva,<sup>41</sup> D. Silvermyr,<sup>27,29</sup> K. S. Sim,<sup>22</sup> C. P. Singh,<sup>3</sup> V. Singh,<sup>3</sup> M. Sivertz,<sup>5</sup> A. Soldatov,<sup>15</sup> R. A. Soltz,<sup>26</sup> W. E. Sondheim,<sup>27</sup> S. P. Sorensen,<sup>46</sup> I. V. Sourikova,<sup>5</sup> F. Staley,<sup>10</sup> P. W. Stankus,<sup>35</sup> E. Stenlund,<sup>29</sup> M. Stepanov,<sup>34</sup> A. Ster,<sup>21</sup> S. P. Stoll,<sup>5</sup> T. Sugitate,<sup>14</sup> J. P. Sullivan,<sup>27</sup> E. M. Takagui,<sup>41</sup> A. Taketani,<sup>38,39</sup> M. Tamai,<sup>50</sup> K. H. Tanaka,<sup>20</sup> Y. Tanaka,<sup>32</sup> K. Tanida,<sup>38</sup> M. J. Tannenbaum,<sup>5</sup> P. Tarján,<sup>11</sup> J. D. Tepe,<sup>1,27</sup> T. L. Thomas,<sup>33</sup> J. Tojo,<sup>24,38</sup> H. Torii,<sup>24,38</sup> R. S. Towell,<sup>1</sup> I. Tserruya,<sup>51</sup> H. Tsuruoka,<sup>48</sup> S. K. Tuli,<sup>3</sup> H. Tydesjö,<sup>29</sup> N. Tyurin,<sup>15</sup> H. W. van Hecke,<sup>27</sup> J. Velkovska,<sup>5,44</sup> M. Velkovsky,<sup>44</sup> L. Villatte,<sup>46</sup> A. A. Vinogradov,<sup>23</sup> M. A. Volkov,<sup>23</sup> E. Vznuzdaev,<sup>37</sup> X. R. Wang,<sup>13</sup> Y. Watanabe,<sup>38,39</sup> S. N. White,<sup>5</sup> F. K. Wohn,<sup>16</sup> C. L. Woody,<sup>5</sup> W. Xie,<sup>6</sup> Y. Yang,<sup>7</sup> A. Yanovich,<sup>15</sup> S. Yokkaichi,<sup>38,39</sup> G. R. Young,<sup>35</sup> I. E. Yushmanov,<sup>23</sup> W. A. Zajc,<sup>9,†</sup> C. Zhang,<sup>9</sup> S. Zhou,<sup>7,51</sup> and L. Zolin<sup>17</sup>

(PHENIX Collaboration)

<sup>1</sup>Abilene Christian University, Abilene, Texas 79699, USA<sup>2</sup>Institute of Physics, Academia Sinica, Taipei 11529, Taiwan<sup>3</sup>Department of Physics, Banaras Hindu University, Varanasi 221005, India<sup>4</sup>Bhabha Atomic Research Centre, Bombay 400 085, India<sup>5</sup>Brookhaven National Laboratory, Upton, New York 11973-5000, USA<sup>6</sup>University of California, Riverside, Riverside, California 92521, USA<sup>7</sup>China Institute of Atomic Energy (CIAE), Beijing, People's Republic of China<sup>8</sup>Center for Nuclear Study, Graduate School of Science, University of Tokyo, 7-3-1 Hongo, Bunkyo, Tokyo 113-0033, Japan<sup>9</sup>Columbia University, New York, New York 10027 and Nevis Laboratories, Irvington, New York 10533, USA<sup>10</sup>Dapnia, CEA Saclay, F-91191 Gif-sur-Yvette, France<sup>11</sup>Debrecen University, H-4010 Debrecen, Egyetem tér 1, Hungary<sup>12</sup>Florida State University, Tallahassee, Florida 32306, USA<sup>13</sup>Georgia State University, Atlanta, Georgia 30303, USA<sup>14</sup>Hiroshima University, Kagamiyama, Higashi-Hiroshima 739-8526, Japan<sup>15</sup>Institute for High Energy Physics (IHEP), Protvino, Russia

- <sup>16</sup>Iowa State University, Ames, Iowa 50011, USA  
<sup>17</sup>Joint Institute for Nuclear Research, 141980 Dubna, Moscow Region, Russia  
<sup>18</sup>KAERI, Cyclotron Application Laboratory, Seoul, South Korea  
<sup>19</sup>Kangnung National University, Kangnung 210-702, South Korea  
<sup>20</sup>KEK, High Energy Accelerator Research Organization, Tsukuba-shi, Ibaraki-ken 305-0801, Japan  
<sup>21</sup>KFKI Research Institute for Particle and Nuclear Physics (RMKI), P. O. Box 49, H-1525 Budapest 114, Hungary  
<sup>22</sup>Korea University, Seoul 136-701, Korea  
<sup>23</sup>Russian Research Center “Kurchatov Institute,” Moscow, Russia  
<sup>24</sup>Kyoto University, Kyoto 606, Japan  
<sup>25</sup>Laboratoire Leprince-Ringuet, Ecole Polytechnique, CNRS-IN2P3, Route de Saclay, F-91128 Palaiseau, France  
<sup>26</sup>Lawrence Livermore National Laboratory, Livermore, California 94550, USA  
<sup>27</sup>Los Alamos National Laboratory, Los Alamos, New Mexico 87545, USA  
<sup>28</sup>LPC, Université Blaise Pascal, CNRS-IN2P3, Clermont-Fd, 63177 Aubiere Cedex, France  
<sup>29</sup>Department of Physics, Lund University, Box 118, SE-221 00 Lund, Sweden  
<sup>30</sup>Institut fuer Kernphysik, University of Muenster, D-48149 Muenster, Germany  
<sup>31</sup>Myongji University, Yongin, Kyonggido 449-728, Korea  
<sup>32</sup>Nagasaki Institute of Applied Science, Nagasaki-shi, Nagasaki 851-0193, Japan  
<sup>33</sup>University of New Mexico, Albuquerque, New Mexico 87131, USA  
<sup>34</sup>New Mexico State University, Las Cruces, New Mexico 88003, USA  
<sup>35</sup>Oak Ridge National Laboratory, Oak Ridge, Tennessee 37831, USA  
<sup>36</sup>IPN-Orsay, Université Paris Sud, CNRS-IN2P3, Boîte Postale 1, F-91406 Orsay, France  
<sup>37</sup>PNPI, Petersburg Nuclear Physics Institute, Gatchina, Russia  
<sup>38</sup>RIKEN (The Institute of Physical and Chemical Research), Wako, Saitama 351-0198, Japan  
<sup>39</sup>RIKEN BNL Research Center, Brookhaven National Laboratory, Upton, New York 11973-5000, USA  
<sup>40</sup>St. Petersburg State Technical University, St. Petersburg, Russia  
<sup>41</sup>Universidade de São Paulo, Instituto de Física, Caixa Postal 66318, São Paulo CEP05315-970, Brazil  
<sup>42</sup>System Electronics Laboratory, Seoul National University, Seoul, South Korea  
<sup>43</sup>Chemistry Department, Stony Brook University, SUNY, Stony Brook, New York 11794-3400, USA  
<sup>44</sup>Department of Physics and Astronomy, Stony Brook University, SUNY, Stony Brook, New York 11794, USA  
<sup>45</sup>SUBATECH (Ecole des Mines de Nantes, CNRS-IN2P3, Université de Nantes) Boîte Postale 20722-44307, Nantes, France  
<sup>46</sup>University of Tennessee, Knoxville, Tennessee 37996, USA  
<sup>47</sup>Department of Physics, Tokyo Institute of Technology, Tokyo 152-8551, Japan  
<sup>48</sup>Institute of Physics, University of Tsukuba, Tsukuba, Ibaraki 305, Japan  
<sup>49</sup>Vanderbilt University, Nashville, Tennessee 37235, USA  
<sup>50</sup>Waseda University, Advanced Research Institute for Science and Engineering, 17 Kikui-cho, Shinjuku-ku, Tokyo 162-0044, Japan  
<sup>51</sup>Weizmann Institute, Rehovot 76100, Israel  
<sup>52</sup>Yonsei University, IPAP, Seoul 120-749, Korea

(Received 8 August 2003; published 30 March 2004)

The PHENIX experiment at the Relativistic Heavy Ion Collider has measured charged hadron yields at midrapidity over a wide range of transverse momenta ( $0.5 < p_T < 10$  GeV/ $c$ ) in Au+Au collisions at  $\sqrt{s_{NN}} = 200$  GeV. The data are compared to  $\pi^0$  measurements from the same experiment. For both charged hadrons and neutral pions, the yields per nucleon-nucleon collision are significantly suppressed in central compared to peripheral and nucleon-nucleon collisions. The suppression sets in gradually and increases with increasing centrality of the collisions. Above 4–5 GeV/ $c$  in  $p_T$ , a constant and almost identical suppression of charged hadrons and  $\pi^0$ 's is observed. The  $p_T$  spectra are compared to published spectra from Au+Au at  $\sqrt{s_{NN}} = 130$  in terms of  $x_T$  scaling. Central and peripheral  $\pi^0$  as well as peripheral charged spectra exhibit the same  $x_T$  scaling as observed in  $p+p$  data.

DOI: 10.1103/PhysRevC.69.034910

PACS number(s): 25.75.Dw

\*Deceased.

†Email address: zajc@nevis.columbia.edu

## I. INTRODUCTION

Lattice quantum chromodynamic (QCD) calculations predict a new state of matter of deconfined quarks and gluons at an energy density exceeding  $\sim 1 \text{ GeV}/\text{fm}^3$  [1]. It has long been suggested that such a “quark gluon plasma” may be produced in collisions between ultrarelativistic heavy nuclei [2]. Indeed, measurements of transverse energy produced in high-energy Pb+Pb and Au+Au collisions suggest that energy densities above  $3 \text{ GeV}/\text{fm}^3$  at the CERN SPS [3] and  $5 \text{ GeV}/\text{fm}^3$  at the Relativistic Heavy Ion Collider (RHIC) [4,5] have been reached. However, this conclusion relies on model assumptions [6–9] to relate the properties of the hadronic final state to the initial state dynamics.

The spectra of high transverse momentum ( $p_T$ ) hadrons resulting from the fragmentation of hard-scattered partons potentially provide a direct probe of the properties of the initial state. Theoretical calculations show that the outgoing high- $p_T$  partons radiate substantially more energy when propagating through dense matter than when propagating in the vacuum, resulting in a softening of the hadron  $p_T$  spectrum [10], with the energy loss of the partons depending on the gluon density of the matter [11,12]. Formation time considerations suggest that hard scattered partons are “produced” at the earliest stage of the collision, thus directly probe the dense matter from the time of their creation. Therefore, a detailed analysis of high- $p_T$  hadron production may reveal information on the properties of the dense medium created early in the collisions [12–14].

At the energies reached at RHIC, high- $p_T$  hadrons are copiously produced. In nucleon-nucleon collisions, it has been well established that hadrons with  $p_T \geq 2 \text{ GeV}/c$  result primarily from the fragmentation of hard-scattered partons, and that the  $p_T$  spectra of these hadrons can be calculated using perturbative QCD (pQCD) [15,16]. Initial measurements of hadron  $p_T$  spectra in Au+Au collisions at  $\sqrt{s_{NN}} = 130 \text{ GeV}$  led to the discovery of a substantial suppression of hadron yields per nucleon-nucleon collision relative to  $pp$  data [17–19]. Data from  $\sqrt{s_{NN}} = 200 \text{ GeV}$  confirm these results [20–23]. The suppression is observed in central but not in peripheral collisions. These observations are consistent with pQCD-inspired modeling of parton energy loss in dense matter [24,25]. However, alternative interpretations that do not assume the formation of a deconfined phase have been proposed based on the modifications of the parton distribution functions in the initial state [26] or final-state hadronic interactions [27].

In addition to hadron suppression, an unexpectedly large fraction of baryons has been observed in central Au+Au collisions for  $p_T$  up to  $4\text{--}5 \text{ GeV}/c$  [28–30], which complicates the interpretation of the high- $p_T$  results. The observed baryon to meson ratio from PHENIX [29] is inconsistent with jet fragmentation in  $p+p$  [31] and  $e^+e^-$  collisions [32]. While the origin of this effect is unclear, it could point towards bulk particle production (“soft physics”) contributing to the  $p_T$  spectra out to  $4\text{--}5 \text{ GeV}/c$ . It has been suggested that coalescence of thermalized quarks combining with energy loss of hard-scattered partons can account for the unusual particle composition, which shifts the region dominated by hard scattering to higher  $p_T$  [33].

Systematic measurements of the  $p_T$ , centrality, particle species, and  $\sqrt{s_{NN}}$  dependence of the suppression can constrain competing descriptions of high- $p_T$  hadron production. In this paper, we present new data on inclusive charged hadron production for  $0.5 < p_T < 10 \text{ GeV}/c$ , measured over a broad range of centrality in Au+Au collisions at  $\sqrt{s_{NN}} = 200 \text{ GeV}$  by the PHENIX Collaboration at RHIC. These data are compared to data on neutral pion production [21] and to data from Au+Au collisions at  $\sqrt{s_{NN}} = 130 \text{ GeV}$  [17,19], all measured within the same experiment.

The remainder of the paper is organized as follows. Section II gives a detailed account of the charged particle analysis. Centrality and  $p_T$  dependence of the charged hadron  $p_T$  spectra are discussed in Sec. III A. Section III B studies the charged hadron suppression and compares the results to  $\pi^0$  data. In Sec. III C, we discuss the  $\sqrt{s_{NN}}$  dependence of both charged hadron and neutral pion production and test possible  $x_T$  scaling. A summary is given in Sec. IV.

## II. DATA ANALYSIS

### A. PHENIX detector

The PHENIX experiment consists of four spectrometer arms—two around midrapidity (the central arms) and two at forward rapidity (the muon arms)—and a set of global detectors. The central arm and south muon arm detectors were completed in 2001 and took data during Au+Au operation of RHIC the same year (RUN-2). The layout of the PHENIX experiment during RUN-2 is shown in Fig. 1. Each central arm covers  $|\eta| < 0.35^\circ$  in pseudorapidity and  $90^\circ$  in azimuthal angle  $\phi$ . In each of the central arms, charged particles are tracked by a drift chamber (DC) positioned from 2.0 to 2.4 m radially outward from the beam axis and two or three layers of pixel pad chambers [PC1, (PC2), PC3 located at 2.4 m, (4.2 m), 5 m in radial direction, respectively]. Particle identification is provided by ring imaging Cerenkov counters (RICH), a time of flight scintillator wall (TOF), and two types of electromagnetic calorimeters (lead scintillator and lead glass). The magnetic field for the central spectrometer is axially symmetric around the beam axis. Its component parallel to the beam axis has an approximately Gaussian dependence on the radial distance from the beam axis, dropping from 0.48 T at the center to 0.096 T (0.048 T) at the inner (outer) radius of the DC. A pair of zero-degree calorimeters (ZDC) and a pair of beam-beam counters (BBC) were used for global event characterization. Further details about the design and performance of PHENIX can be found in Ref. [34].

### B. Event selection

During RUN-2, PHENIX sampled an integrated luminosity of  $24 \mu\text{b}^{-1}$  for Au+Au collisions at  $\sqrt{s_{NN}} = 200 \text{ GeV}$ . Minimum bias events were selected by a coincidence between the ZDCs and the BBCs. This selection corresponds to  $92.2_{-3.0}^{+2.5}\%$  of the  $6.9 \text{ b}$  Au+Au inelastic cross section. The event centrality is determined by correlating the charge detected in the BBCs with the energy measured in the ZDCs. Two sets of centrality definitions are used in this analysis: a

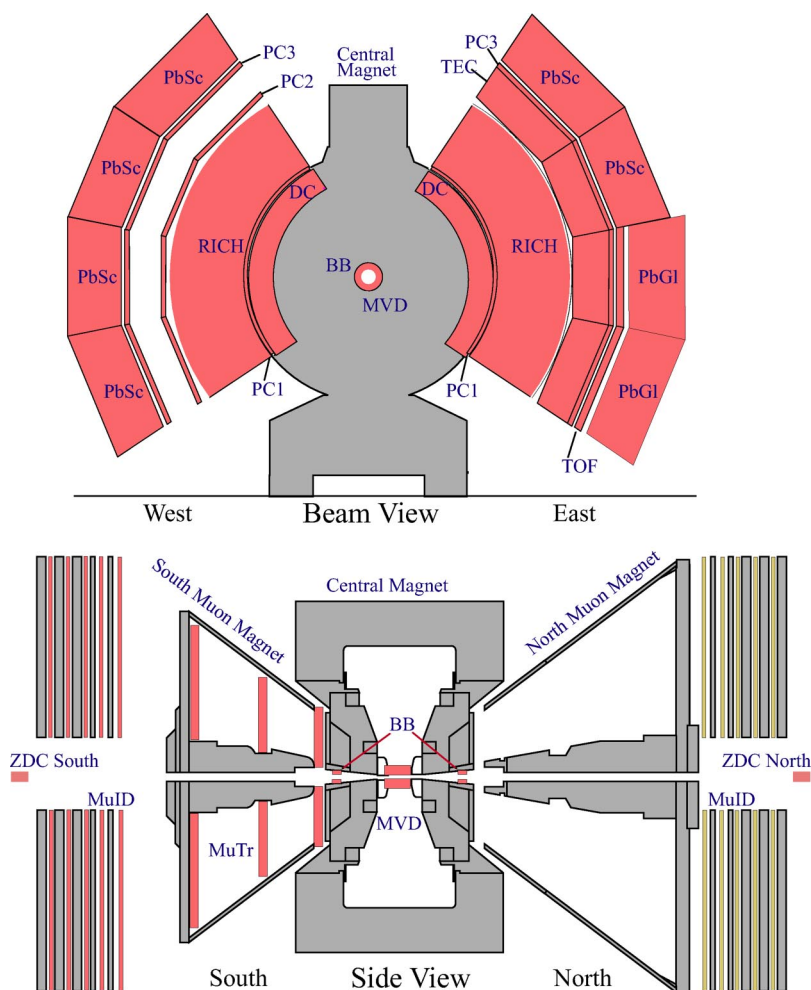


FIG. 1. (Color online) PHENIX experimental layout for the Au+Au run in 2001. The top panel shows the PHENIX central arm spectrometers viewed along the beam axis. The bottom panel shows a side view of the PHENIX muon arm spectrometers.

“Fine” set of centralities, which corresponds to 0–5%, ..., 15–20%, 20–30%, ..., 80–92%, and a “Coarse” set of centralities, which corresponds to 0–10%, 10–20%, 20–30%, ..., 80–92%. A Glauber model Monte Carlo simulation [35–38] that includes the responses of BBC and ZDC gives an estimate of the average number of binary collisions  $\langle N_{coll} \rangle$ , participating nucleons  $\langle N_{part} \rangle$ , and nuclear overlap function  $\langle T_{AuAu} \rangle$  for each centrality class. The calculated values of  $\langle N_{coll} \rangle$ ,  $\langle N_{part} \rangle$ , and  $\langle T_{AuAu} \rangle$  for each centrality class are listed in Table I.

In addition to the event selection, the BBCs also allow us to reconstruct the collision vertex in the beam direction ( $z$ ) with a resolution of 0.5 cm. An offline  $z$ -vertex cut,  $|z_{vtx}| < 30$  cm, was applied to the minimum bias events. After this selection, a total of  $27 \times 10^6$  minimum bias Au+Au events were analyzed to obtain the charged hadron spectra presented in this paper.

### C. Charged particle tracking and momentum measurement

Charged hadron tracks are measured using information from the DC, PC1, PC2, and PC3 detectors of the west central arm and the BBC. The projections of the charged particle trajectories into a plane perpendicular to the beam axis are detected typically in 12 wire planes in the DC. The wire

planes are spaced at 0.6 cm intervals along the radial direction from the beam axis. Each wire provides a projective measurement, with better than  $150 \mu\text{m}$  spacial resolution in the azimuthal ( $\phi$ ) direction. Eight additional wire planes in the DC provide stereoscopic projections, which together with the space point measured at the PC1 and the vertex position measured by the BBC determine the polar angle of the track. Trajectories are confirmed by requiring matching hits at both PC2 and PC3 to reduce the secondary background.

Tracks are then projected back to the collision vertex through the magnetic field to determine the momentum  $\vec{p}$ . The transverse momentum  $p_T$  is related to the deflection angle  $\alpha$  measured at the DC with respect to an infinite momentum trajectory. For tracks emitted perpendicular to the beam axis, this relation can be approximated by

$$\alpha \approx \frac{K}{p_T}, \quad (1)$$

where  $K=87$  mrad GeV/ $c$  is the effective field integral.

The momentum scale is verified by comparing the known proton mass to the value measured for charged particles identified as protons from their time of flight. The flight time is measured in the TOF detector, which cover  $\pi/4$  of the

TABLE I. Centrality classes, average number of  $N+N$  collisions, average number of participant nucleons, and average nuclear overlap function obtained from a Glauber Monte Carlo simulation of the BBC and ZDC responses for Au+Au at  $\sqrt{s_{NN}}=200$  GeV. Each centrality class is expressed as a percentage of  $\sigma_{AuAu}=6.9$  b. Two sets of centrality definitions are used in this analysis: a ‘‘Fine’’ set of centralities, which corresponds to 0–5%, ..., 15–20%, 20–30%, ..., 80–92%, and a ‘‘Coarse’’ set of centralities, which corresponds to 0–10%, 10–20%, 20–30%, ..., 80–92%.

Centrality (%)	$\langle N_{coll} \rangle$	$\langle N_{part} \rangle$	$\langle T_{AuAu} \rangle$ (mb $^{-1}$ )
0–5	1065±105.5	351.4±2.9	25.37±1.77
5–10	854.4±82.1	299±3.8	20.13±1.36
10–15	672.4±66.8	253.9±4.3	16.01±1.15
15–20	532.7±52.1	215.3±5.3	12.68±0.86
0–10	955.4±93.6	325.2±3.3	22.75±1.56
10–20	602.6±59.3	234.6±4.7	14.35±1.00
20–30	373.8±39.6	166.6±5.4	8.90±0.72
30–40	219.8±22.6	114.2±4.4	5.23±0.44
40–50	120.3±13.7	74.4±3.8	2.86±0.28
50–60	61.0±9.9	45.5±3.3	1.45±0.23
60–70	28.5±7.6	25.7±3.8	0.68±0.18
70–80	12.4±4.2	13.4±3.0	0.30±0.10
80–92	4.9±1.2	6.3±1.2	0.12±0.03
60–92	14.5±4	14.5±2.5	0.35±0.10
Minimum bias	257.8±25.4	109.1±4.1	6.14±0.45

azimuthal acceptance in the east arm. The absolute value of the momentum scale is known to be correct to better than 0.7%.

The momentum resolution is directly related to the  $\alpha$  resolution,

$$\delta p/p = \delta\alpha/\alpha = \frac{1}{K} \sqrt{\left(\frac{\sigma_{ms}}{\beta}\right)^2 + (\sigma_{\alpha} p)^2}, \quad (2)$$

where  $\delta\alpha$  is the measured angular spread, which can be decomposed into the contribution from multiple scattering  $\sigma_{ms}$  and the contribution from the intrinsic pointing resolution  $\sigma_{\alpha}$  of the DC. At high  $p_T$ ,  $\sigma_{\alpha}$  is the dominating contribution, i.e.,  $\delta\alpha \approx \sigma_{\alpha}$ . We measure  $\sigma_{\alpha} \approx 0.84 \pm 0.05$  mrad/(GeV/c) using zero field data, where we select high-momentum tracks by requiring energetic hadronic showers in the electromagnetic calorimeters. The width of the proton mass as function of  $p_T$  independently confirms the momentum resolution. In summary, the momentum resolution is determined to be  $\delta p/p \approx 0.7\% \oplus 1.0\% p$  (GeV/c). Further details on track reconstruction and momentum determination can be found in Ref. [39].

#### D. Background rejection and subtraction

Approximately 95% of the tracks reconstructed by the DC originate from the event vertex. The remainder have to be investigated as potential background to the charged particle measurement. The main background sources include secondary particles from decays and  $e^+e^-$  pairs from the conversion

of photons in materials between the vertex and the DC. Depending on how close the conversion or decay point is to the DC, or depending on the  $Q$  value of the decay, these tracks may have a small deflection angle  $\alpha$  at the DC. Thus, according to Eq. (1), they are incorrectly assigned a large momentum. In this analysis, the  $p_T$  range over which charged particle production is accessible in PHENIX is limited by this background. We exploit the track match to PC2 and PC3 to reject as much of the background as possible, then employ a statistical method to measure and subtract the irreducible background.

For primary tracks, the distance in both the  $r-\phi$  and the  $z$  direction between the track projection point and the measured PC hit position is approximately Gaussian with a mean of 0 and a width given by

$$\sigma_{match} = \sqrt{\sigma_{det}^{match2} + \left(\frac{\sigma_{ms}^{match}}{p\beta}\right)^2}, \quad (3)$$

where  $\sigma_{det}^{match}$  is the finite detector resolution [which includes DC pointing (or  $\alpha$ ) resolution and the PC2, PC3 spacial resolution], and  $\sigma_{ms}^{match}$  is the multiple scattering contribution.

Despite being incorrectly reconstructed with large  $p_T$ , the majority of the background particles have low momenta. While traveling from the DC to the PC2 and PC3, they multiple scatter and receive an additional deflection from the fringe field. This causes a correlated deflection between the measured positions at PC2, PC3, and the projections calculated from tracks measured by the DC and PC1. The displacements in  $r-\phi$  and  $z$  directions are represented by  $D_{\phi}$  and  $D_z$ . Since the residual bend depends on the  $z$  component of the fringe field, which decreases rapidly at large  $|\eta|$ , a fiducial cut of  $|\eta| < 0.18$  was applied to ensure that the residual bend due to the fringe field is almost independent of  $z$ .

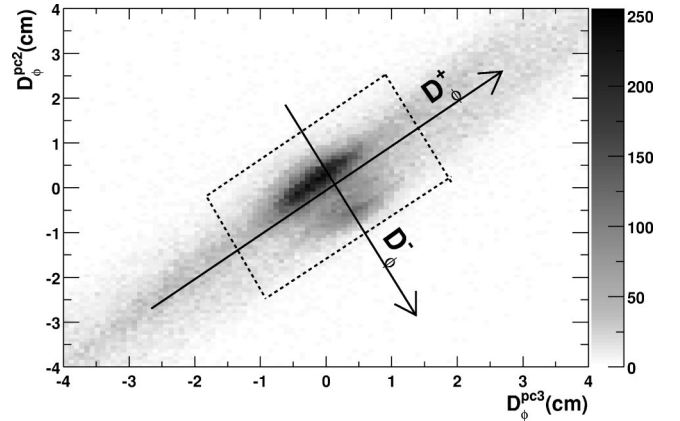


FIG. 2.  $D_{\phi}^{pc2}$  (the difference between projection and hit location in  $r-\phi$  direction at PC2) vs  $D_{\phi}^{pc3}$  in centimeters for tracks with reconstructed  $p_T > 4$  GeV/c. PC2, PC3 matching differences are correlated, with signal tracks peaked around 0 and background tracks extend along the  $D_{\phi}^+$  direction. The double-peak structure along  $D_{\phi}^-$  is related to the finite granularity of PC2 and PC3 pads. The positive directions of  $D_{\phi}^+$  and  $D_{\phi}^-$  are indicated by the arrow.  $A \pm 2\sigma$  cut on these variables is illustrated by the box region inside the dashed lines.

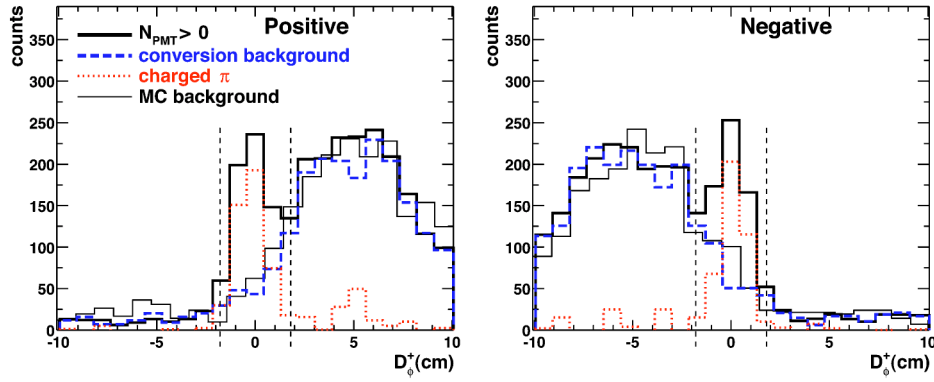


FIG. 3. (Color online) Background contamination due to electrons, illustrated by the track match in  $D_\phi^+$  for tracks with associated RICH PMTs and  $6 < p_T < 7$  GeV/c. The matching distributions are shown for minimum bias events and separately for positive (left) and negative (right) charged tracks. The first three distributions represent the raw counts for all tracks with RICH association (thick solid line), estimated conversion backgrounds (dashed line), and charged pions (dot-dashed line) that were obtained by subtracting the dashed line from the solid line. The thin solid line represents the matching distribution of background electrons from Monte Carlo simulation, arbitrarily scaled to match the data. The  $\pm 2\sigma$  matching windows are illustrated by the vertical dashed line. Since  $e^+$  and  $e^-$  are deflected in opposite directions by the fringe field, they are shifted to positive and negative directions, respectively.

We focus on the displacement in  $r-\phi$ ,  $D_\phi$ , which are large for low momentum tracks due to the residual bend. The  $D_\phi$ 's at PC2 and PC3 are correlated with each other, as shown in Fig. 2. Most of the tracks lie in a narrow window around the diagonal line. The width of this window is given by the PC2 and PC3 detector resolutions, which are of the order of a few millimeters. Multiple scattering and residual bend broaden the matching distribution along the diagonal line. To optimize background rejection, we define two orthogonal projections,

$$D_\phi^+ = \frac{1}{\sqrt{2}}(D_\phi^{pc2} + D_\phi^{pc3}),$$

$$D_\phi^- = \frac{1}{\sqrt{2}}(D_\phi^{pc2} - D_\phi^{pc3}). \quad (4)$$

$D_\phi^+$  is the variable along the correlated direction,  $D_\phi^-$  is the direction normal to  $D_\phi^+$ . A  $\pm 2\sigma$  cut on these variables is applied in the data analysis. In the remaining discussion, unless stated otherwise, only tracks satisfying these cuts are included.

After matching cuts, the background level is less than 6% for  $p_T < 4$  GeV/c, but increases rapidly at higher  $p_T$ . For  $4 < p_T < 10$  GeV/c, the most significant remaining background sources are  $e^+e^-$  from conversion of photons close to the DC and particles from weak decays of long lived particles, mainly of  $K^\pm$  and  $K_L^0$ . These backgrounds are estimated and subtracted separately from the  $D_\phi^+$  distribution for all tracks, as will be discussed in the rest of this section.

To separate the two background sources, we take advantage of the RICH to tag electrons. Charged particles with velocities above the Cherenkov threshold  $\gamma_{th}=35$  (CO<sub>2</sub> radiator) will emit Cherenkov photons, which are detected by photon multiplier tubes (PMTs) in the RICH [40]. We characterize the Cherenkov photon yield for a charged particle by  $N_{PMT}$ , the number of PMTs with signals above threshold as-

sociated with the track. For reconstructed electrons ( $p_T > 150$  MeV/c), the average number of associated PMTs is  $\langle N_{PMT} \rangle \approx 4.5$ . The probability to find at least one PMT above threshold is more than 99%. For pions, the Cherenkov threshold is 4.8 GeV/c, and the number of associated PMTs reaches its asymptotic value only well above 10 GeV/c;  $\langle N_{PMT} \rangle$  increases from 1.4 at 6 GeV/c to 2.8 at 8 GeV/c and 3.6 at 10 GeV/c.

Tracks ( $N_R$ ) with at least one associated RICH PMT contain both conversion electrons and real pions. Their matching distributions in  $D_\phi^+$  are presented in Fig. 3 for a sample range of  $6 < p_T < 7$  GeV/c. Also shown is the matching distribution for conversion electrons from Monte Carlo simulation. The contributions from pions and electrons are clearly distinguishable. For pions with  $p_T < 10$  GeV/c,  $\langle N_{PMT} \rangle$  has not reached its asymptotic value. A requirement of  $N_{PMT} \geq 5$  rejects most of the pions while preserving a well-defined fraction ( $R_e$ ) of the electrons. To measure  $R_e$  from the data, we select tracks with an apparent  $p_T > 10$  GeV/c.<sup>1</sup> The fraction of tracks with  $N_{PMT} \geq 5$  is measured to be  $R_e = 0.458 \pm 0.05$ . Both Monte Carlo and data show a small variation of  $R_e$  with  $p_T$  and centrality. This variation is included in the error on  $R_e$ . The total electron background is calculated using tracks with  $N_{PMT} \geq 5$  ( $N_e$ ) as,  $N_e/R_e$ . The number of real pions in the RICH-associated sample for each  $p_T$  bin is then calculated as

$$S_R = N_R - \frac{N_e}{R_e}. \quad (5)$$

With this method, a small fraction of genuine pions, which satisfy  $N_{PMT} \geq 5$ , is subtracted. This fraction is negligible

<sup>1</sup>In this  $p_T$  range, the background yield decreases slowly with  $p_T$ , while the true  $\pi$  yield decreases rapidly as  $p_T$  increases. By comparing the measured  $\pi^0$  spectrum from PHENIX [21] with the charged hadron spectrum before background subtraction at  $p_T > 10$  GeV/c, the integrated signal yield is estimated to be less than 3% and thus may be neglected.

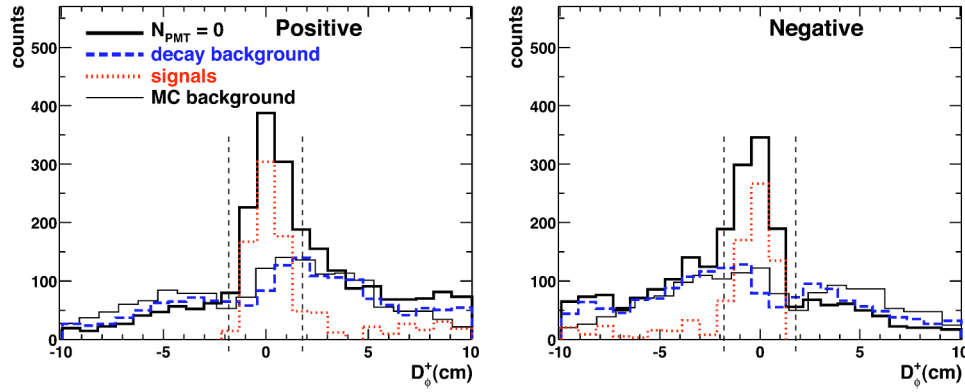


FIG. 4. (Color online) Background contamination due to decays, illustrated by the track match in  $D_\phi^+$  for tracks without an associated RICH PMT and with  $6 < p_T < 7$  GeV/c, shown for minimum bias events and separately for positive (left) and negative (right) charged tracks. The first three distributions represent the raw counts for all tracks without RICH association (thick solid line), estimated decay backgrounds (dashed line), and signal tracks (dot-dashed line) that were calculated as the difference of the two. The thin solid line represents the matching distribution of decay background from Monte Carlo simulation, arbitrarily scaled to match the data. The two  $\pm 2\sigma$  matching windows are illustrated by the vertical dashed line. Outside the signal window, the shape of the dashed line matches the solid line rather well, the difference of 10% level is taken into account in the error estimation of  $R_{decay}$ .

below 7 GeV/c, but increases rapidly towards higher  $p_T$ . This loss is corrected using the PHENIX Monte Carlo simulation. In this case, a 100% error on the correction is assigned.

The sample of tracks ( $N_{NR}$ ) with no associated RICH PMT contains a mixture of  $\pi, K, p$ , contaminated by the decay background. Their matching distributions in  $D_\phi^+$  are shown in Fig. 4 for  $6 < p_T < 7$  GeV/c, together with the matching distribution for decay particles from MC simulation. A Monte Carlo study shows that the apparent momentum of these tracks is nearly uncorrelated with true momentum and therefore the distribution of this background in  $D_\phi^+$  is nearly independent of the apparent momentum. We select a nearly pure background sample using tracks with reconstructed  $p_T > 10$  GeV/c and measure the ratio of the number of tracks passing a  $|D_\phi^+| < 2\sigma$  cut to tracks in the interval  $3\sigma < |D_\phi^+| < 9\sigma$ :

$$R_{decay} = \frac{N_{NR}(p_T > 10 \text{ GeV}/c, |D_\phi^+| < 2\sigma)}{N_{NR}(p_T > 10 \text{ GeV}/c, 3\sigma < |D_\phi^+| < 9\sigma)} = 0.424 \pm 0.05. \quad (6)$$

The error quoted takes into account the small variation of  $R_{decay}$  with  $p_T$  and centrality. Since the average yield of real hadrons in this interval is small, we estimate the decay contribution as a function of  $p_T$  to be  $N_{NR}(3\sigma < |D_\phi^+| < 9\sigma) \times R_{decay}$ . Finally, the signal is calculated as

$$S_{NR} = N_{NR}(|D_\phi^+| < 2\sigma) - N_{NR}(3\sigma < |D_\phi^+| < 9\sigma) \times R_{decay}. \quad (7)$$

Figure 5 gives the total signal, obtained as  $S_R + S_{NR}$ , with the decay and conversion background subtracted. On the right hand side, the signal-to-background ratio is shown. The

background increases with increasing  $p_T$ . At 4 GeV/c the signal-to-background ratio is about 10, and decreases to 1 at 7.5 GeV/c and to  $\sim 0.3$  at 10 GeV/c.

Weak decays of short lived particles, mainly  $K_s^0, \Lambda,$  and  $\bar{\Lambda}$  within the magnetic field provide an additional source of background. A significant fraction of this background is subtracted using the  $R_{decay}$  method described above. However, secondary particles from decays close to the event vertex are not subtracted since they are nearly indistinguishable from primary particles. This “feed-down” contaminates the track sample without the associated RICH PMTs,  $S_{NR}$  (about 40% of all charged particles at high  $p_T$ ), and needs to be subtracted from the data.

To estimate the feed-down contribution we generate Au + Au events with HIJING [41], reconstruct them through the PHENIX Monte Carlo simulation, and count the secondaries which survive all analysis cuts. The secondaries from  $\Lambda$  and  $\bar{\Lambda}$  decays are counted relative to the reconstructed  $(p + \bar{p})$ , and correspondingly, those from  $K_s^0$  relative to  $(K^+ + K^-)/2$ . We tune the  $(\Lambda + \bar{\Lambda})/(p + \bar{p}), K_s^0/[0.5(K^+ + K^-)]$  ratios by weighting the particle distributions generated according to HIJING such that they reproduce the nearly  $p_T$  independent experimentally observed ratios from Au+Au collisions at  $\sqrt{s_{NN}} = 130$  GeV [42,43].

The final feed-down contribution depends on the choice of the  $\Lambda$  and  $K_s^0$   $p_T$  spectra and of their yields in the high- $p_T$  range where they are not measured. Both yields and spectral shapes are varied within limits imposed by the spectrum for tracks that do not fire the RICH. The average feed-down contribution depends on  $p_T$  and varies between 6% to 13% relative to the total charged hadron yield; it is subtracted from the charged spectra. The systematic uncertainties are estimated from the spread of the feed-down contributions obtained with different assumptions. The uncertainties are approximately 60% of the subtraction, and depend on  $p_T$  and centrality.

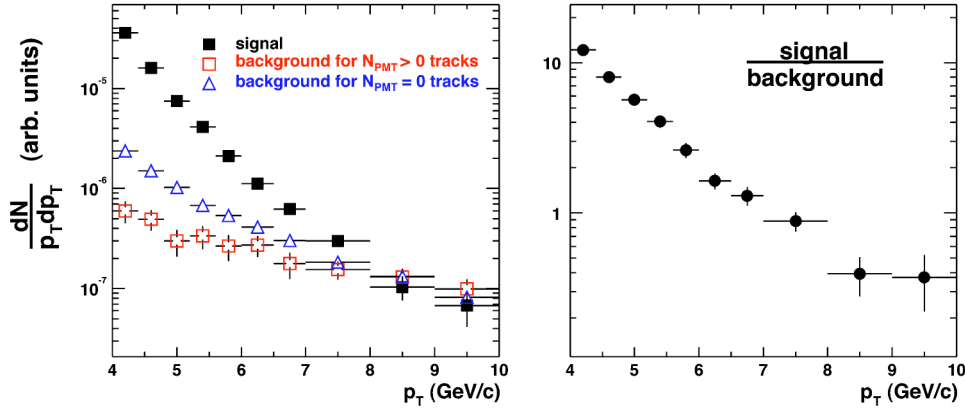


FIG. 5. (Color online) Amount of background estimated as a function of  $p_T$  for minimum bias collision. The left part shows the background subtracted charged hadron spectra (filled square), the background from  $\gamma$  conversions (open square), and decays (open triangle). The right part shows the signal to background ratio. Only statistical errors are shown.

Table II summarizes the systematic errors on the background subtraction.<sup>2</sup> All errors are correlated with  $p_T$  and are presented as relative errors to the charged hadron yield. The uncertainty on the pion oversubtraction correction ( $\delta_{\pi loss}$ ) was rescaled by the fraction of signal tracks with RICH association, i.e.,  $S_R/(S_R+S_{NR})$ . Errors on the scaling factors  $R_e$  and  $R_{decay}$  were individually folded with the signal-to-background ratios in the two samples. The resulting uncertainties on the charged yields were then added in quadrature ( $\delta_{R_e \oplus R_{decay}}$ ). The uncertainty of the  $K_s^0$ ,  $\Lambda$ , and  $\bar{\Lambda}$  feed-down subtraction is denoted by  $\delta_{feeddown}$ .

### E. Corrections and systematic uncertainties

After background subtraction, we have determined a single,  $p_T$ -dependent correction function to correct the hadron spectra for acceptance, decay in flight, reconstruction efficiency, and momentum resolution. This function is determined using a GEANT [44] Monte Carlo simulation [45] of the PHENIX detector in which simulated single tracks are reconstructed using the same analysis chain applied to the real data. Because of decays and multiple scattering, the correction function depends on the particle species. This is reflected in Fig. 6, where the correction functions averaged between  $\pi^+$  and  $\pi^-$ ,  $K^+$  and  $K^-$ ,  $p^+$  and  $p^-$  are shown separately. At  $p_T < 3$  GeV/c, the kaon correction function is significantly larger than those for pions and protons. For  $p_T > 3$  GeV/c, this difference is less than 15%. To take into account this species dependence, we determine the correction function separately for pions, kaons, protons, and their anti-particles. The final correction function is then obtained by combining the correction functions for the different particle species weighted by the measured  $p_T$ -dependent particle composition from Ref. [46]. Above 2 GeV/c, where kaon data are not available, we assume the  $K/\pi$  ratio is constant within  $\pm 10\%$  from the value observed at 2 GeV/c. This assumption leads to a 2.5% systematic error in the correction function. The resulting correction function is plotted in the upper left panel of Fig. 7. The sharp rise below 2 GeV/c is due to loss in acceptance and decays in flight. Above

2 GeV/c, the correction decreases only slowly with  $p_T$ . For  $p_T > 4$  GeV/c, the correction varies by less than  $\pm 5\%$ .

The data are also corrected for efficiency losses due to detector occupancy. Though this is negligible for peripheral collisions, these losses are important in central collisions, and are evaluated by embedding simulated tracks into real events. The average track reconstruction efficiency in the active detector area is larger than 98% for peripheral collisions, but decreases to  $(70 \pm 3.5)\%$  for central collisions. As shown in the lower part of Fig. 7, the efficiency loss is independent of  $p_T$  within a  $\pm 3\%$  systematic uncertainty from 1.5 to 10 GeV/c. Based on this observation, the full correction can be factorized into centrality-dependent (i.e., detector occupancy dependent) correction function  $c(N_{part})$ , and  $p_T$ -dependent correction function  $c(p_T)$ . The centrality-dependent correction function is shown on the upper right panel of Fig. 7. Most of the efficiency loss is due to hit overlaps, which can shift the hit positions in the DC or PC's outside of the matching windows. The  $\pm 2\sigma$  matching windows are larger at low  $p_T$  to account for multiple scattering [see Eq. (3)], thus the tracks are less vulnerable to the effect of hit merging. This effect has been taken into account by applying a slightly smaller,  $p_T$ -dependent, occupancy correction at  $p_T < 1.5$  GeV/c.

Figure 7 also shows systematic errors on the correction functions. These errors include not only the errors on the correction itself, but also the uncertainty due to the background subtraction procedure.

Finally, the inclusive charged hadron yield is obtained by multiplying the  $p_T$ -dependent correction function  $c(p_T)$  and centrality-dependent correction function  $c(N_{part})$  with the background subtracted spectra and dividing by the number of events for every centrality class as

$$\frac{1}{N_{evts}} \frac{dN}{2\pi p_T dp_T d\eta} = \frac{1}{N_{evts}} \times c(p_T) \times c(N_{part}) \times \left( \frac{dN}{p_T dp_T d\eta} \right)^{bgr-subtracted}. \quad (8)$$

The systematic errors on the spectra, which are common to all centrality classes, are listed in Table III. Sources of systematic uncertainties are the matching cuts ( $\delta_{match}$ ), normalization ( $\delta_{norm}$ ), particle composition ( $\delta_{mix}$ ), momentum

<sup>2</sup>We should emphasize that, in the remaining discussion unless stated otherwise, all systematic errors listed in tables have been adjusted to  $1\sigma$  errors.

TABLE II. Systematic errors on background subtraction. All errors are given in percent and are quoted as  $1\sigma$  errors. These errors are correlated with  $p_T$ .

$p_T$ (GeV/c)	$\delta_{\pi_{loss}}$ (%)	$\delta_{R_e \oplus R_{decay}}$ (%)	$\delta_{feeddown}$ (%)	Total (%)
<5	0.3	0.3	5	5
5–6	0.6	1.8	5	5.3
6–7	1.4	4.1	8.5	9.5
7–8	4.6	7.1	7.8	11.5
8–9	9.9	17.6	6	21.1
9–10	19.4	23.5	6	31.1

resolution ( $\delta_{reso}$ ), momentum scale ( $\delta_{scale}$ ), and background subtraction ( $\delta_{bgr}$ ) from Table II. The normalization error is independent of  $p_T$ . All other errors vary with  $p_T$  but are highly correlated bin-to-bin, which means that points in neighboring  $p_T$  bins can move in the same direction by similar factors.

The centrality-dependent systematic errors are quantified in terms of the central-to-peripheral ratio  $R_{cp}$ , as given in Table IV. Besides the uncertainty on the occupancy correction ( $\delta_{occupancy}$ ) illustrated in Fig. 7, the background subtraction procedure has a centrality-dependent uncertainty. As discussed in Sec. II D, the errors on  $R_e$  and  $R_{decay}$  reflect the  $p_T$  and centrality dependencies. The centrality-dependent part contributes about half of the error on both  $R_e$  and  $R_{decay}$ , and hence does not cancel in  $R_{cp}$ . Since the errors on  $R_e$  and  $R_{decay}$  are independent, the uncertainty on  $R_{cp}$  is approximately equal to  $\delta_{R_e \oplus R_{decay}}$  from Table II. Finally,  $\delta_{feeddown}$  is the centrality-dependent error from feed-down subtraction.

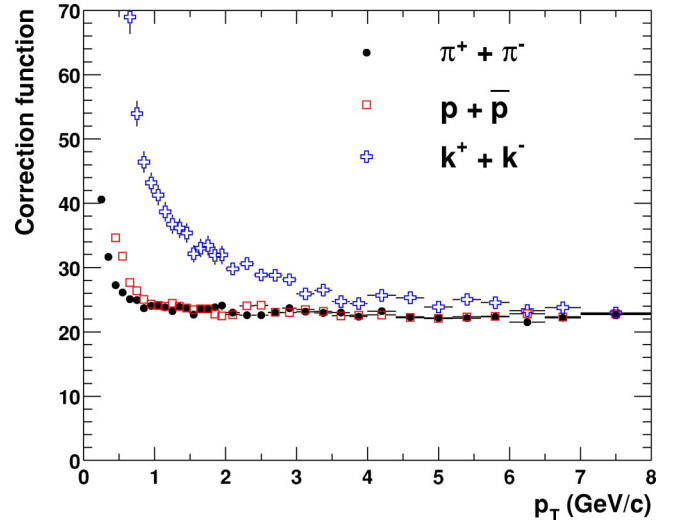


FIG. 6. (Color online) Averaged correction functions for  $\pi^+$  and  $\pi^-$ ,  $p$  and  $\bar{p}$ , and  $K^+$  and  $K^-$ .

### III. RESULTS

#### A. Inclusive charged hadron $p_T$ spectra

Figure 8 shows the inclusive charged hadron  $p_T$  spectra for various centrality classes. All spectra exhibit power-law tails at high  $p_T$ . But for peripheral collisions, the power-law shape is more concave than for central collisions. More details of the centrality dependence of the spectral shape can be seen from Fig. 9, which shows for each centrality class the ratio of the spectra to the minimum-bias spectrum. In these ratios, most systematic errors cancel or affect the overall scale only. The characteristic centrality dependence of the shape already observed in  $\sqrt{s_{NN}}=130$  GeV Au+Au collisions

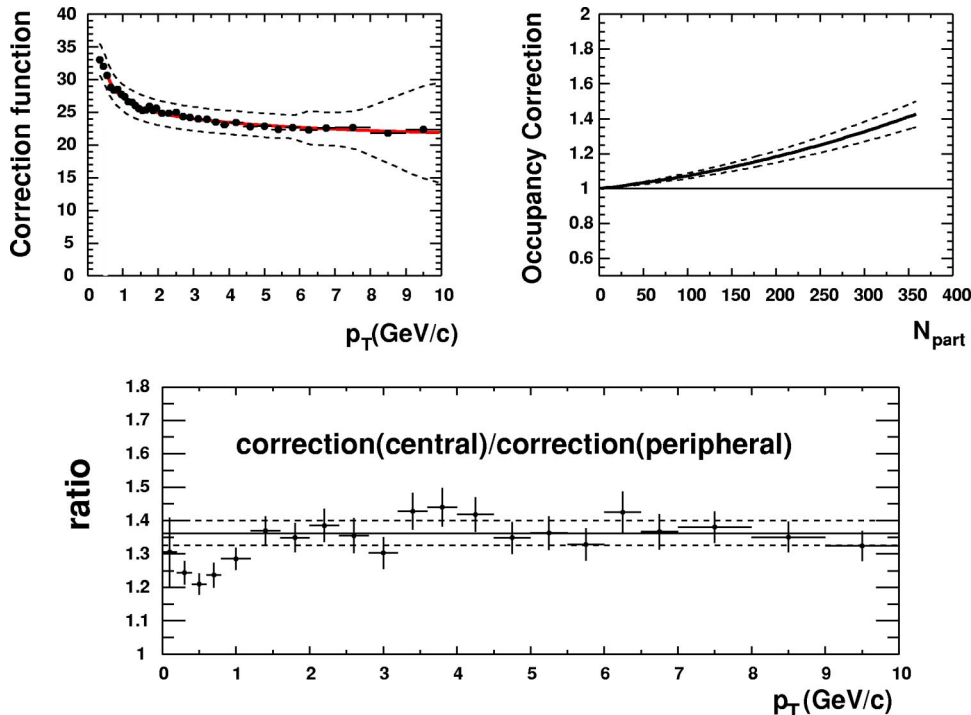


FIG. 7. (Color online) Functions used to correct the charged particle  $p_T$  spectra. The upper left panel shows the  $p_T$ -dependent correction  $c(p_T)$ . The upper right panel shows the centrality dependent correction  $c(N_{part})$ . Systematic uncertainties are indicated by the dashed lines. The two corrections factorize at  $p_T > 1.5$  GeV/c, so that for given centrality the full correction function is given by  $c(p_T) \times c(N_{part})$ . The accuracy of this factorization is demonstrated in the lower panel. The ratio of the full correction for central collisions (5% most central) to the correction for single particle events varies by less than 3% above 1.5 GeV/c (the error bar is the statistical error from the Monte Carlo calculation).

TABLE III. Systematic errors on the  $p_T$  spectra. All errors are given in percent and are quoted as  $1\sigma$  errors. They are either normalization errors or are  $p_T$  correlated errors.

$p_T$ (GeV/c)	$\delta_{match}$ (%)	$\delta_{norm}$ (%)	$\delta_{mix}$ (%)	$\delta_{reso}$ (%)	$\delta_{scale}$ (%)	$\delta_{bgr}$ (%)	Total (%)
<1	3.5	3.2	2.4	0.6	0.6	5	7.3
1–5	3	3.2	2.4	0.6	3	5	7.6
5–6	3	3.2	1.8	0.6	3.6	5.3	7.9
6–7	3	3.2	1.8	0.6	3.3	9.5	11.1
7–8	3	3.2	1.8	0.6	3.1	11.5	12.8
8–9	3	3.2	1.8	0.9	3.1	21.1	21.9
9–10	3	3.2	1.8	5.3	3.1	31.1	32.1

[18,19] is more apparent at  $\sqrt{s_{NN}}=200$  GeV. In peripheral collisions, the ratio decreases up to  $p_T \sim 2$  GeV/c and then rises up to about 4 GeV/c. The trends are reversed in the most central collisions. In the range above 4–5 GeV/c, all ratios appear to be constant as a function of  $p_T$ , which would imply that they have a similar centrality independent shape.

Based on the different trends observed in Fig. 9, we can distinguish three  $p_T$  regions: 0.5–2, 2–4.5, and  $>4.5$  GeV/c. The different centrality dependence of the spectral shape in these regions can be quantified by a truncated average  $p_T$ :

$$\langle p_T^{trunc} \rangle \equiv \frac{\int_{p_T^{min}}^{8 \text{ GeV/c}} p_T dN/dp_T}{\int_{p_T^{min}}^{8 \text{ GeV/c}} dN/dp_T} - p_T^{min}, \quad (9)$$

which is insensitive to the normalization of the spectra. The upper bound of 8 GeV/c in the integral is given by the limited  $p_T$  reach for peripheral centrality classes as shown in Fig. 8. In Fig. 10, the values of  $\langle p_T^{trunc} \rangle$  for the three  $p_T^{min}$  values are plotted as a function of centrality, represented by the average number of participating nucleons ( $N_{part}$ ) for each centrality class.

For  $p_T^{min}=0.5$  GeV/c, where particle production is expected to be governed by soft physics,  $\langle p_T^{trunc} \rangle$  increases with  $N_{part}$ . This trend is also seen for the average  $p_T$  of identified charged hadrons, and reflects the increased radial flow of soft particles in more central collisions [46]. For  $p_T^{min}=2$  GeV/c,

TABLE IV. Systematic errors on the central-to-peripheral ratio. All errors are given in percent and are quoted as  $1\sigma$  errors. Most of the systematic errors listed in Table III cancel in the central-to-peripheral ratio. Only those errors that are uncorrelated with centrality are shown here.

$p_T$ (GeV/c)	$\delta_{occupancy}$ (%)	$\delta_{feeddown}$ (%)	$\delta_{R_e \oplus R_{decay}}$ (%)	Total (%)
<6	5	5	1.8	7.3
6–7	5	5	4.1	8.2
7–8	5	5	7.1	10
8–9	5	5	17.6	19
9–10	5	5	23.5	24.6

the trend is significantly different. For peripheral collisions,  $\langle p_T^{trunc} \rangle$  is substantially larger than the value obtained with  $p_T^{min}=0.5$  GeV/c due to the presence of the power-law tail. With increasing  $N_{part}$ ,  $\langle p_T^{trunc} \rangle$  for  $p_T^{min}=2$  GeV/c decreases and the values obtained with  $p_T^{min}=0.5$  and 2 GeV/c approach each other, which indicates an almost exponential spectrum in central collisions between 0.5 and 2 GeV/c. For the highest  $p_T$  range ( $p_T^{min}=4.5$  GeV/c),  $\langle p_T^{trunc} \rangle$  is approximately constant. This implies that the shape of the spectrum is nearly independent of centrality, as would be expected if this region is dominated by hard scattering.

However, the yields at high  $p_T$  do not scale with the number of nucleon-nucleon collisions; they are suppressed comparing to the binary collision scaling expected for hard scattering processes. This can be clearly seen from Fig. 11, which shows  $R_{cp}$ , the ratio of yields for central and peripheral collisions normalized to the average number of nucleon-nucleon collisions in each event sample. The ratio is below unity for all  $p_T$ . The three  $p_T$  regions show different trends as outlined in the discussion of Fig. 10.

(i) In the “soft” region with  $p_T < 2$  GeV/c, the ratio increases as a function of  $p_T$ .

(ii) In the “hard” region with  $p_T > 4.5$  GeV/c, the suppression appears to be constant at  $\sim 0.3$ , which again indicates that the spectra have a similar shape, but with the yield in central collisions being suppressed by a constant factor from 4.5 to 10 GeV/c.

(iii) In the transition region from 2 to  $\sim 4.5$  GeV/c, the ratio decreases as a function of  $p_T$ .

### B. Suppression of high- $p_T$ hadrons in Au+Au at $\sqrt{s_{NN}}=200$ GeV

At finite  $Q^2$ , nuclear modifications of the parton distribution [26,47] and initial [48] and final state [10] interactions of the scattering partons can modify the high- $p_T$  hadron production rates in hard scattering processes. Medium modifications of hadron spectra are often quantified by the “nuclear modification factor”  $R_{AA}$ , which we calculate for each centrality class as the ratio of the yield per nucleon-nucleon collision in Au+Au to the yield in nucleon-nucleon collisions:

$$R_{AA}(p_T, \eta) = \left( \frac{1}{N_{evt}} \frac{d^2 N^{A+A}}{dp_T d\eta} \right) / \left( \frac{\langle N_{coll} \rangle}{\sigma_{inel}^{N+N}} \frac{d^2 \sigma^{N+N}}{dp_T d\eta} \right), \quad (10)$$

$\langle N_{coll} \rangle / \sigma_{inel}^{N+N}$  is the average Glauber nuclear overlap function,  $\langle T_{AuAu} \rangle$ , for each centrality class. In order to calculate  $R_{AA}$ ,

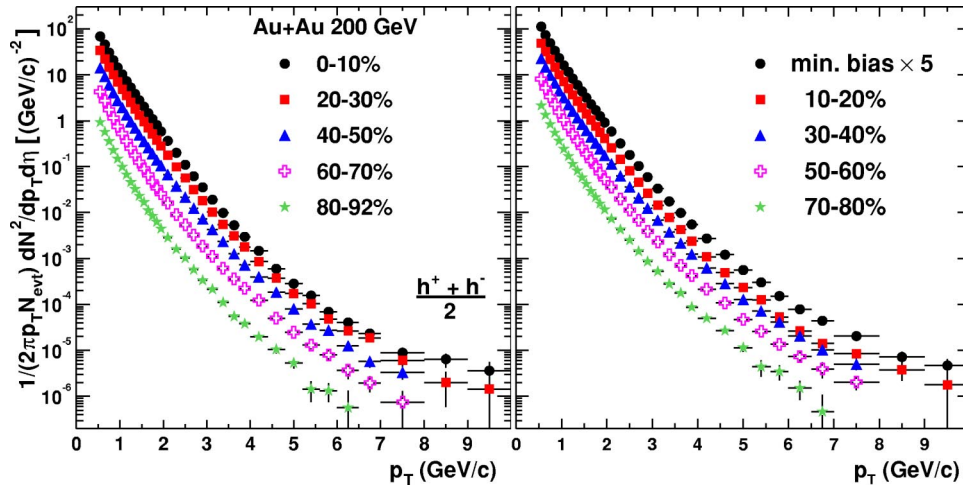


FIG. 8. (Color online)  $p_T$  spectra of charged hadrons for minimum bias collisions along with spectra for nine centrality classes derived from the pseudorapidity region  $|\eta| < 0.18$ . The minimum bias spectrum has been multiplied by 5 for visibility. Only statistical errors are shown in the spectra. Most of the  $p_T$ -dependent systematic errors are independent of centrality and are tabulated in Table III.

we need a reference spectrum for nucleon-nucleon collisions. Due to the lack of charged hadron data with sufficient reach in  $p_T$  from our own experiment, we construct the  $N+N$  reference for charged hadrons from the  $\pi^0$  spectra in  $p+p$  collisions at  $\sqrt{s}=200$  GeV/c measured by PHENIX [16], and the charged hadron to pion ratio observed in other experiments, as described below.

The PHENIX  $\pi^0$  spectra from  $p+p$  collisions are measured out to 14 GeV/c. These data can be parametrized by a power-law function,

$$\frac{1}{2\pi p_T} \frac{d^2 \sigma_{N+N}^{\pi^0}}{dp_T d\eta} = A \left( \frac{p_0}{p_0 + p_T} \right)^n, \quad (11)$$

with  $A=386$  mb/(GeV/c)<sup>2</sup>,  $p_0=1.219$  GeV/c, and  $n=9.99$  [16].

In  $p+p$  experiments at the ISR, the  $h/\pi$  ratio was measured to be  $1.6 \pm 0.16$ , independent of  $p_T$  from 1.5 to 5 GeV/c, and independent of  $\sqrt{s}$  from 23 to 63 GeV [31]. Below 1.5 GeV/c,  $h/\pi$  decreases towards lower  $p_T$ . The ISR data are consistent with data on  $\pi, K, P$  production from FNAL E735 experiment [49] at  $\sqrt{s}=1.8$  TeV. The  $h/\pi$  ratio computed from these data increases with  $p_T$  and reaches a value of 1.6 at the end of the measured  $p_T$  range,  $\sim 1.5$  GeV/c. At high momentum, a  $h/\pi$  ratio of  $\sim 1.6$  is

also observed for quark and gluon jet fragmentation in  $e^+e^-$  collisions at LEP by the DELPHI Collaboration [32]. Finally, charged hadron data measured by PHENIX in  $p+p$  collisions and data measured by UA1 [50] in  $\bar{p}+p$  collisions, both at  $\sqrt{s}=200$  GeV/c, give consistent  $h/\pi$  ratios when compared to the PHENIX  $p+p$   $\pi^0$  data.

Based on these findings, we assume that  $h/\pi$  is constant above 1.5 GeV/c in  $p+p$  collisions at RHIC and that we can scale up the  $\pi^0$  cross section [Eq. (11)] by this factor to obtain a reference for charged hadron production. To be consistent with the data described above, we correct this reference below 1.5 GeV/c using an empirical function,

$$r(p_T) = \begin{cases} R_{h/\pi} - a(p_{max} - p_T)^2 & \text{for } p_T \leq p_{max} \\ R_{h/\pi} & \text{for } p_T > p_{max}, \end{cases} \quad (12)$$

where  $R_{h/\pi}=1.6$ ,  $p_{max}=1.6$  GeV/c, and  $a=0.28$  (GeV/c)<sup>-2</sup>. The charged hadron reference used in this analysis is then given by the product of the power-law function from Eq. (11) and the empirical correction from Eq. (12) as

$$\frac{1}{2\pi p_T} \frac{d^2 \sigma_{N+N}^{h^+h^-}}{dp_T d\eta} = A \left( \frac{p_0}{p_0 + p_T} \right)^n \times r(p_T). \quad (13)$$

The systematic errors on the charged hadron  $N+N$  reference are summarized in Table V. The main sources of uncer-

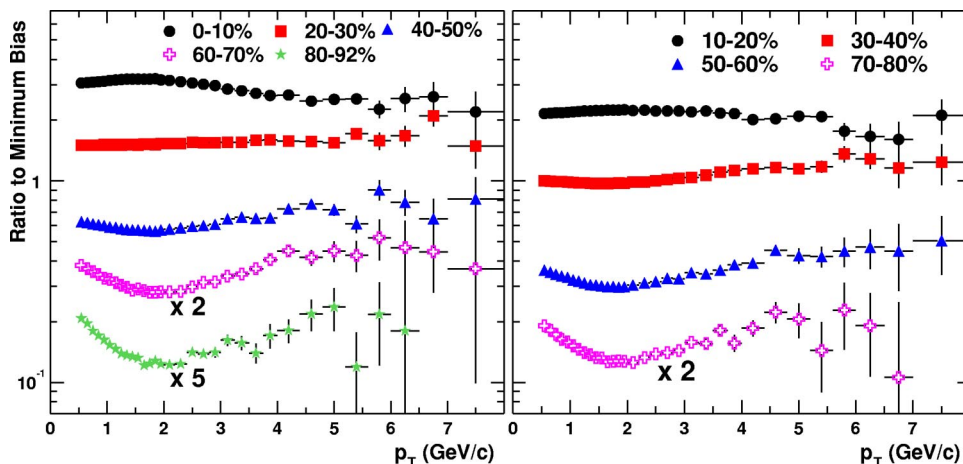


FIG. 9. (Color online) Ratios of centrality selected  $p_T$  spectra to the minimum bias spectrum. Ratios for peripheral classes are scaled up for clarity. For the  $p_T$  range shown, most of the systematic errors cancel in the ratio. The remaining systematic errors that can change the shape are less than 10% (see Table IV) and are correlated bin-to-bin in  $p_T$ .

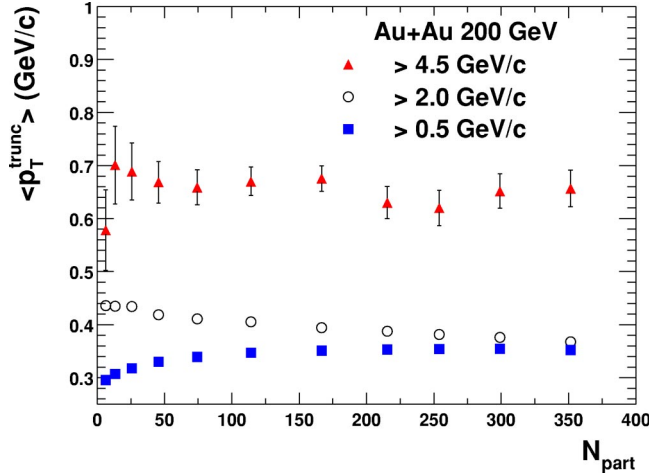


FIG. 10. (Color online) Centrality dependence of  $\langle p_T^{trunc} \rangle$ , the average  $p_T$  of charged particles above a  $p_T$  threshold as defined in Eq. (9). Shown are  $\langle p_T^{trunc} \rangle$  values for three  $p_T^{min}$  cuts, with  $p_T^{min} = 0.5, 2,$  and  $4.5$  GeV/c, respectively. The errors shown are statistical only. The systematical errors for all data points are less than 3%.

tainties include: (i) the systematic errors on the absolute normalization of the PHENIX  $\pi^0$  data ( $\delta_{norm}^{\pi^0}$ ), which are independent of  $p_T$ ; (ii) uncertainties due to the power-law fit to the  $\pi^0$  data ( $\delta_{fit}^{\pi^0}$ ); and (iii) uncertainties on  $R_{h/\pi}$  ( $\delta_{h/\pi}$ ), which are estimated from the spread of  $R_{h/\pi}$  obtained from different data sets used to constrain  $h/\pi^0$ .

Figure 12 shows the nuclear modification factor  $R_{AA}(p_T)$  for charged hadrons from minimum bias and nine centrality classes. The systematic errors on  $R_{AA}$  are described in the

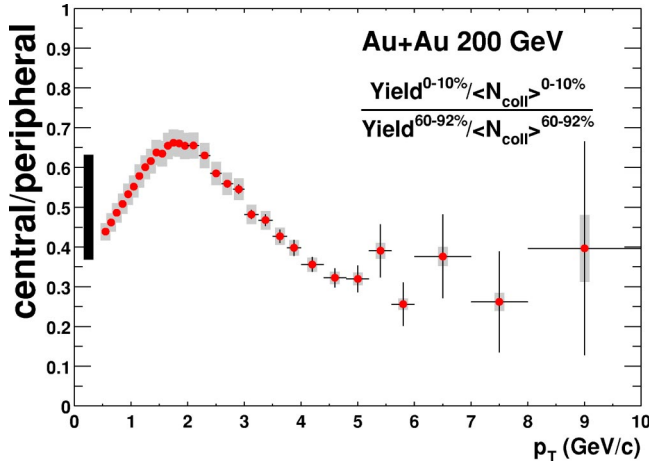


FIG. 11. (Color online) Ratio of charged hadron yields per nucleon-nucleon collision between central (0–10%) and peripheral (60–92%) Au+Au collisions. The solid error bars on each data point are statistical. The error bar on the left hand side of the figure is the overall scale error relative to 0.5, which is the quadrature sum of (i) the uncertainty of  $\langle N_{coll} \rangle$  (see Table I) and (ii) the uncertainty on the occupancy correction ( $\delta_{occupancy}$ ). The shaded error band on each data point is the  $p_T$ -dependent systematic error from  $\delta_{R_e \otimes R_{decay}}$  and centrality dependent feed down correction ( $\delta_{feeddown}$ ) as given in Table IV.

TABLE V. Systematic errors on the charged hadron  $N+N$  reference spectrum. All errors are given in percent and are quoted as  $1\sigma$  errors. Positive and negative errors are given separately where appropriate. Most of the errors are correlated with  $p_T$ .

$p_T$ (GeV/c)	$\delta_{norm}^{\pi^0}$ (%)	$\delta_{fit}^{\pi^0}$ (%)	$\delta_{R_{h/\pi}}$ (%)	Total (%)
0.75	$\pm 10.4$	$-3.9+9.1$	$-15.1+5.9$	$-18.7+15.0$
1.00	$\pm 10.4$	$-4.1+8.9$	$-14.4+5.9$	$-18.3+14.9$
1.50	$\pm 10.4$	$-4.6+8.3$	$-11.6+5.9$	$-16.3+14.6$
2.00	$\pm 10.4$	$-5.1+7.7$	$-7.9+5.9$	$-14.0+14.2$
2.50	$\pm 10.4$	$-5.5+7.2$	$-5.9+5.9$	$-13.1+13.9$
3.00	$\pm 10.4$	$-5.9+6.7$	$-5.9+5.9$	$-13.3+13.7$
3.50	$\pm 10.4$	$-6.4+6.4$	$-5.9+5.9$	$-13.5+13.5$
4.50	$\pm 10.4$	$-7.5+6.5$	$-5.9+5.9$	$-14.1+13.6$
5.50	$\pm 10.4$	$-8.9+7.9$	$-5.9+5.9$	$-14.9+14.3$
6.50	$\pm 10.4$	$-10.7+10.5$	$-5.9+5.9$	$-16.0+15.9$
7.50	$\pm 10.4$	$-12.9+14.3$	$-5.9+5.9$	$-17.6+18.7$
8.50	$\pm 10.4$	$-15.8+19.4$	$-5.9+5.9$	$-19.8+22.8$
9.50	$\pm 10.4$	$-19.3+25.9$	$-5.9+5.9$	$-22.7+28.5$

figure captions. At low  $p_T$ , the charged hadron  $R_{AA}$  increase monotonically up to 2 GeV/c for all centrality classes. At  $p_T > 2$  GeV/c,  $R_{AA}$  remains constant and close to unity for the most peripheral centrality class. However, in central collisions, it decreases at higher  $p_T$ , down to an approximately constant value of 0.2–0.3 for  $p_T > 4$ –5 GeV/c. This is consistent with Fig. 11, where the central to peripheral ratio also saturates above 4–5 GeV/c. This approximately  $p_T$  independent suppression pattern has been interpreted as a result of the detailed interplay between the Cronin effect, nuclear shadowing, and partonic energy loss [51].

Also shown in Fig. 12 are  $R_{AA}$  for neutral pions from Ref. [21]. The neutral pion  $R_{AA}$  values also seem to reach maximum around 2 GeV/c, but the changes are smaller than those for charged hadrons. Except for the most peripheral bin, the neutral pion  $R_{AA}$  are always below the charged  $R_{AA}$  in the range of  $2 < p_T < 4.5$  GeV/c. However, at  $p_T > 4.5$  GeV/c,  $R_{AA}$  for both neutral pions and hadrons saturate at roughly the same level, indicating a similar suppression for neutral pions and charged hadrons at high  $p_T$ .

The fact that the neutral pion  $R_{AA}$  values are smaller than inclusive charged hadron  $R_{AA}$  at intermediate  $p_T$  ( $2 < p_T < 4.5$  GeV/c) has already been observed at  $\sqrt{s_{NN}} = 130$  GeV [17]. This difference can be explained by the large  $p/\pi$  ratio observed in the same  $p_T$  range in central Au+Au collisions [28,29]. This large relative proton and antiproton yield indicates a deviation from the standard picture of hadron production at  $p_T > 2$  GeV/c, which assumes that the hadrons are created by the fragmentation of energetic partons. Such a deviation has led to models of quark coalescence [33] or baryon junctions [52] as the possible mechanisms to enhance the proton production rate at medium  $p_T$ . Both models predict that baryon enhancement is limited to  $p_T < 5$  GeV/c, beyond which jet fragmentation should eventually become the dominant production mechanism for all particle species. In that case, one would expect a similar

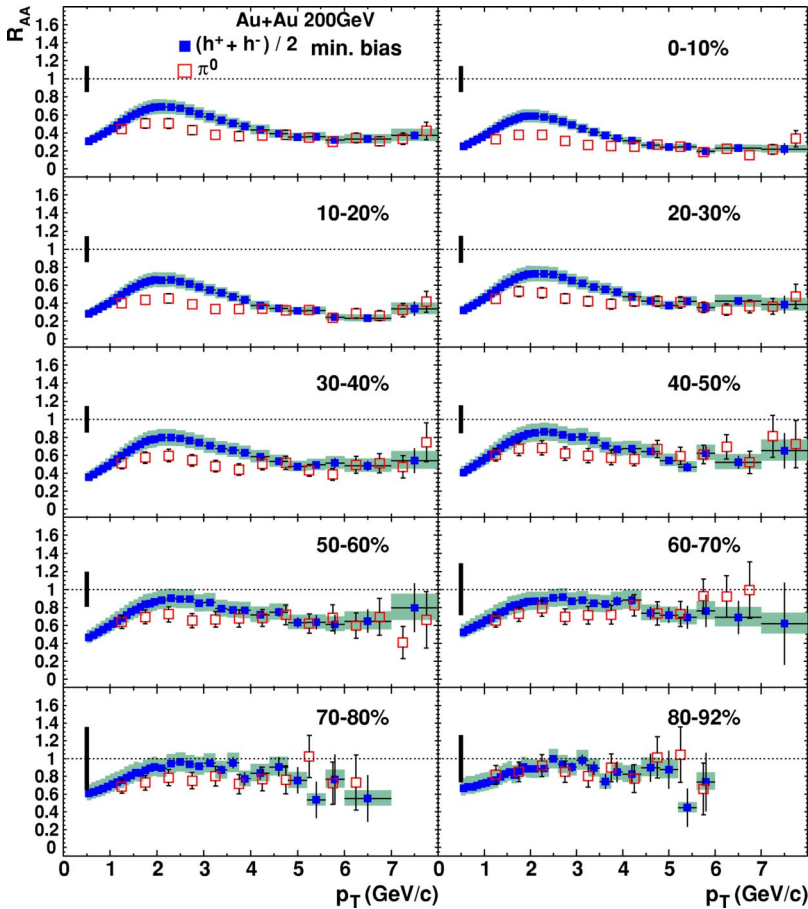


FIG. 12. (Color online)  $R_{AA}$  for  $(h^+ + h^-)/2$  and  $\pi^0$  as a function of  $p_T$  for minimum bias and nine centrality classes according to the “Fine” type of centrality classes defined in Table I. The error bars on the  $\pi^0$  data points include statistical and systematic errors on the Au+Au data and the  $N+N$  reference. The error bars on  $(h^+ + h^-)/2$  data points are statistical errors only. The common normalization errors ( $\delta_{norm}^{\pi^0}$  from Table V) on the references for charged hadrons and  $\pi^0$ 's are added in quadrature with the uncertainty on  $\langle N_{coll} \rangle$  and are indicated by the black bar on the left side of each panel. This error ranges from 15% to 36% from central to peripheral collisions and can shift all points in the charged and neutral pion  $R_{AA}$  up and down together. The shaded band on charged  $R_{AA}$  includes the remaining systematic errors on the charged  $N+N$  reference summed in quadrature with the systematic errors from the Au+Au spectra. This error amounts to  $-12.5\% + 18\%$  at low  $p_T$  and changes to  $\pm 12.5\%$  at  $p_T = 4.5$  GeV/c and  $\pm 18.5\%$  at  $p_T = 8$  GeV/c.

suppression factor for charged hadron and  $\pi^0$ , in agreement with the data at  $p_T > 4.5$  GeV/c. Recently, the difference of  $R_{AA}$  between charged hadrons and pions was also argued as the consequence of centrality and particle species dependent  $\langle k_T \rangle$  broadening effect [53].

If hard-scattering dominates charged hadron production at  $p_T > 4.5$  GeV/c, the particle composition should be determined by the jet fragmentation function, similar to nucleon-nucleon collisions. Figure 13 shows  $h/\pi^0$  for all centrality classes. The systematic errors are explained in the figure captions. In the most peripheral collisions, the  $h/\pi^0$  ratio is consistent with the  $p+p$  values down to  $p_T \approx 2$  GeV/c. In central collisions, the  $h/\pi^0$  ratio is enhanced by as much as 50% above the  $p+p$  value in the region  $1 < p_T < 4.5$  GeV/c. This enhancement gradually decreases towards more peripheral collisions and reflects the difference of  $R_{AA}$  between the charged hadrons and  $\pi^0$ 's, which is due to large baryon contribution. The enhancement also strongly depends on  $p_T$ . It reaches a maximum between 2.5 and 3.5 GeV/c, then decreases. At  $p_T > 4.5$  GeV/c, the  $h/\pi^0$  ratios for all centralities reach an approximately constant value of 1.6, which is consistent with the  $h/\pi$  value observed in  $p+p$  [31] collisions and in jet fragmentation in  $e^+e^-$  [32] collisions. The similarity of the spectral shape and of the particle composition between Au+Au and  $p+p$  collisions suggest that fragmentation of hard-scattered partons is the dominant mechanism of particle production in Au+Au collisions above  $p_T$  of 4–5 GeV/c, regardless of the fact that the yields do not scale with  $N_{coll}$ .

Since  $R_{AA}$  values for charged hadrons and  $\pi^0$ 's are approximately constant at  $p_T > 4.5$  GeV/c, we can quantify the centrality dependence of the  $R_{AA}$  value by calculating it from yields integrated above 4.5 GeV/c. The upper panel of Fig. 14 shows  $R_{AA}$  for  $p_T > 4.5$  GeV/c as a function of  $N_{part}$ . The  $R_{AA}$  values for charged hadrons and  $\pi^0$  agree for all centrality classes within errors. In peripheral collisions with  $N_{part} < 50$ ,  $R_{AA}$  is consistent with binary collision scaling. With increasing  $N_{part}$ ,  $R_{AA}$  decreases monotonically, reaching a value of  $0.23 \pm 0.03$  (0–5% most central) for charged hadrons and  $0.24 \pm 0.02$  (0–10% most central) for  $\pi^0$ 's. There is an additional 14% error common to charged hadrons and  $\pi^0$ 's, which originates from the uncertainty on the  $N+N$  reference and  $N_{coll}$ .

To address suggestions that the yield of high- $p_T$  hadrons in Au+Au collisions may be proportional to  $N_{part}$  instead of  $N_{coll}$  [26,54], we have investigated a different ratio,

$$R_{AA}^{N_{part}} = 2\langle N_{coll} \rangle / \langle N_{part} \rangle \times R_{AA}. \quad (14)$$

$R_{AA}^{N_{part}}$  for  $p_T > 4.5$  GeV/c is shown in the lower panel of Fig. 14, together with solid (or dashed) bands representing the allowed range if the data follow binary collision (or participant) scaling. As discussed above, for peripheral collisions,  $R_{AA}^{N_{part}}$  follows more closely the binary collision scaling. Above 50 participants,  $R_{AA}^{N_{part}}$  varies by only  $\pm 20\%$ .

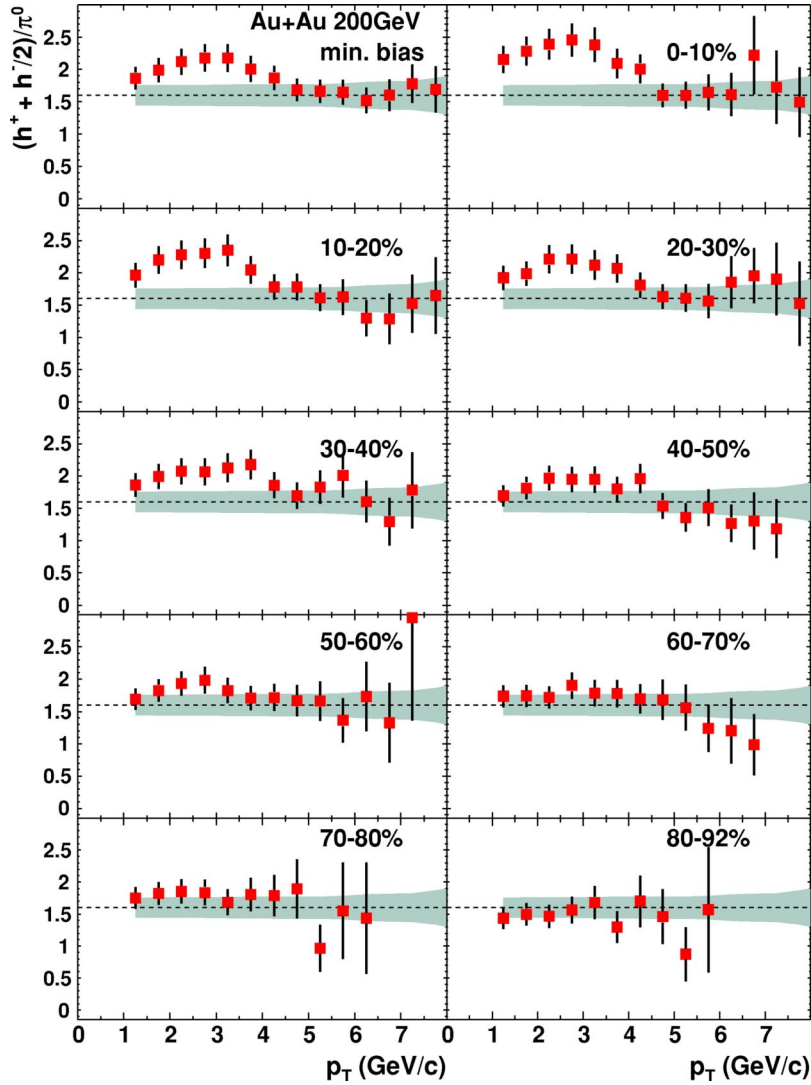


FIG. 13. (Color online) Charged hadron to  $\pi^0$  ratios for minimum bias events and nine centrality classes according to the “Fine” type of centrality classes defined in Table I. The error bars represent the quadratic sum of statistical and point-by-point systematic errors from  $(h^+ + h^-)/2$  and  $\pi^0$ . The shaded band shows the percent normalization error [dominantly from  $(h^+ + h^-)/2$  data] common to all centrality classes. The dashed line at 1.6 is the  $h/\pi$  ratio measured in  $p+p$  [31] and  $e^+e^-$  [32] collisions.

However, it peaks at  $\langle N_{part} \rangle = 100$  and decreases monotonically towards more central collisions.<sup>3</sup>

The decrease of  $R_{AA}^{N_{part}}$  could be a natural consequence of the energy loss of hard scattered partons in the medium [54]. If the energy loss is large, hard scattered partons may only escape near the surface of the reaction volume. In a cylindrical collision geometry, for which the number of collisions from the surface is proportional to  $N_{part}$ , binary collision scaling is reduced to an approximate participant scaling. Detailed calculations show that in this case,  $R_{AA}^{N_{part}}$  slightly decreases with  $N_{part}$  depending in details on how the energy loss is modeled [54]. This interpretation is also consistent with our previous conclusion that, above 4.5 GeV/c, hadron production is dominated by hard scattering although the

yield does not scale with the number of binary collisions. Gluon saturation scenarios [26] also suggest approximate participant scaling, with a 30% increase in  $R_{AA}$  over the  $p_T$  range 4.5–9 GeV/c in central collisions. This increase cannot be excluded by the data.

### C. Energy dependence and $x_T$ scaling

The inclusive charged hadron and  $\pi^0 p_T$  spectra and  $h/\pi^0$  ratios suggest that fragmentation of hard scattered partons is the dominant production mechanism of high- $p_T$  hadrons not only in  $p+p$  but also in Au+Au collisions. For  $p+p$  collisions this fact was demonstrated on general principles well before the advent of QCD by the method of “ $x_T$  scaling.” This method does not depend on whether the initial projectiles are protons or Au ions, so it should be directly applicable to Au+Au collisions. Since our data show a suppression of high- $p_T$  particles in central Au+Au collisions with respect to pointlike scaling from  $p+p$  and peripheral Au+Au collisions, it is important to investigate whether the production dynamics of high- $p_T$  particles in central (and peripheral) Au+Au collisions are the same or different from those in  $p+p$  collisions. We first review the  $x_T$ -scaling method in  $p+p$  collisions and then apply it to the present Au+Au data.

<sup>3</sup>In the  $p_T$  range from 3–4 GeV/c,  $R_{AA}^{N_{part}}$  for charged hadrons is approximately constant, which is consistent with earlier measurements at  $\sqrt{s_{NN}}=130$  GeV [19] and  $\sqrt{s_{NN}}=200$  GeV [20]. To interpret this constancy as participant scaling is misleading, since pion and proton yields change differently with centrality in this  $p_T$  region, and  $R_{AA}^{N_{part}}$  accidentally appears constant for inclusive charged hadron. The data above 4.5 GeV/c shown in Fig. 14 are free of this effect.

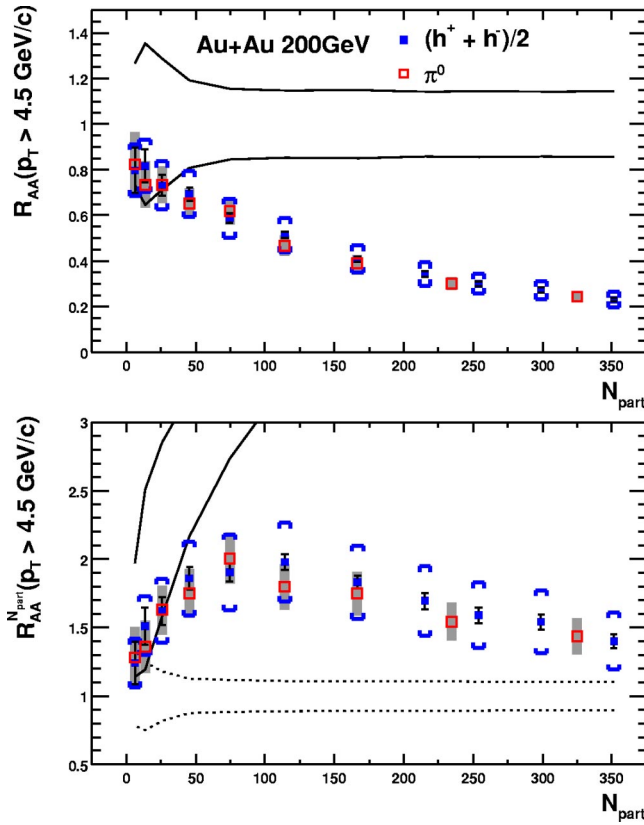


FIG. 14. (Color online) Au+Au yield integrated for  $p_T > 4.5$  GeV/c over the  $N+N$  yield, normalized using either  $N_{coll}$  ( $R_{AA}$  in the top panel) or  $N_{part}$  ( $R_{AA}^{N_{part}}$  in the bottom panel), plotted as a function of  $\langle N_{part} \rangle$ . The bands represent the expectation of binary collisions (solid) and participant pair (dashed) scaling. The width of the bands gives the systematic errors on  $N_{coll}(N_{part})$  added in quadrature with the common normalization errors on the  $N+N$  references for charged hadrons and neutral pions. For charged hadrons, the statistical errors are given by the bars. The systematic errors, which are not common with the errors for neutral pions and which are correlated in  $p_T$ , are shown as brackets. The shaded bars around each neutral pion point represent the systematic and statistical errors; these errors are not correlated with the errors shown for the charged hadron data.

The idea of hard scattering in  $N+N$  collisions dates from the first indication of pointlike structure inside the proton, in 1968, found in deep inelastic electron-proton scattering [55], i.e., scattering with large values of four-momentum transfer squared  $Q^2$  and energy loss  $\nu$ . The discovery that the deep inelastic scattering (DIS) structure function

$$F_2(Q^2, \nu) = F_2\left(\frac{Q^2}{\nu}\right) \quad (15)$$

“scales,” or in other words, depends on the ratio

$$x = \frac{Q^2}{2M\nu} \quad (16)$$

independent of  $Q^2$  as suggested by Bjorken [56], led to the concept of a proton being composed of pointlike “partons.” Since the partons of DIS are charged, and hence must scatter

electromagnetically from each other in  $p+p$  collisions, a general formula for the cross section of the single-particle inclusive reaction

$$p + p \rightarrow C + X \quad (17)$$

was derived [57] using the principle of factorization of the reaction into parton distribution functions for the protons, fragmentation functions to particle  $C$  for the scattered partons, and a short-distance parton-parton hard scattering cross section.

The invariant cross section for the single-particle inclusive reaction [Eq. (17)], where particle  $C$  has transverse momentum  $p_T$  near midrapidity, was given by the general scaling form [58]

$$E \frac{d^3\sigma}{dp^3} = \frac{1}{p_T^n} F\left(\frac{2p_T}{\sqrt{s}}\right) \quad \text{where} \quad x_T = 2p_T/\sqrt{s}. \quad (18)$$

The cross section has two factors: a function  $F$  which depends only on the ratio of momenta, and a dimensioned factor  $p_T^{-n}$ , where  $n$  depends on the quantum exchanged in the hard-scattering. For QED or vector gluon exchange [57],  $n = 4$ . For the case of quark-meson scattering by the exchange of a quark [58],  $n = 8$ . The discovery of high- $p_T$  pions in  $p+p$  scattering at the CERN-ISR, in 1972 [59–61], at a rate much larger than predicted by electromagnetic scattering, but with the scaling form of Eq. (18), proved that the partons of DIS strongly interact with each other.

Inclusion of QCD [62] into the scaling form [Eq. (18)] led to the  $x_T$ -scaling law,

$$E \frac{d^3\sigma}{dp^3} = \frac{1}{\sqrt{s}^{n(x_T, \sqrt{s})}} G(x_T), \quad (19)$$

where the “ $x_T$ -scaling power”  $n(x_T, \sqrt{s})$  should equal 4 in lowest order (LO) calculations, analogous to the  $1/q^4$  form of Rutherford scattering in QED. The structure and fragmentation functions, which scale as the ratios of momenta are all in the  $G(x_T)$  term. Due to higher order effects such as the running of the coupling constant,  $\alpha_s(Q^2)$ , the evolution of the structure and fragmentation functions, and the initial state  $k_T$ , measured values of  $n(x_T, \sqrt{s})$  in  $p+p$  collisions are in the range from 5 to 8.

The compilation of single particle inclusive transverse momentum spectra at midrapidity from  $p+p$  and  $p+\bar{p}$  collisions at center-of-mass (c.m.) energy  $\sqrt{s}$  from 23 to 1800 GeV [31,50,63,64] is shown in Fig. 15(a) for  $(h^+ + h^-)/2$ , and in Fig. 16(a) for  $\pi^0$  [16,65–68]. The spectra exhibit a characteristic shape: an exponential part at low  $p_T \leq 1$  GeV/c which depends very little on  $\sqrt{s}$  (soft physics), and a power-law tail for  $p_T \geq 2$  GeV/c which depends very strongly on  $\sqrt{s}$  (hard physics). The high- $p_T$  part of the spectra shows a characteristic scaling behavior indicative of fragmentation of jets produced by hard scattering of the quark and gluon constituents of the proton as described by QCD [69–71].

The  $x_T$  scaling of the single particle inclusive data is nicely illustrated by a plot of

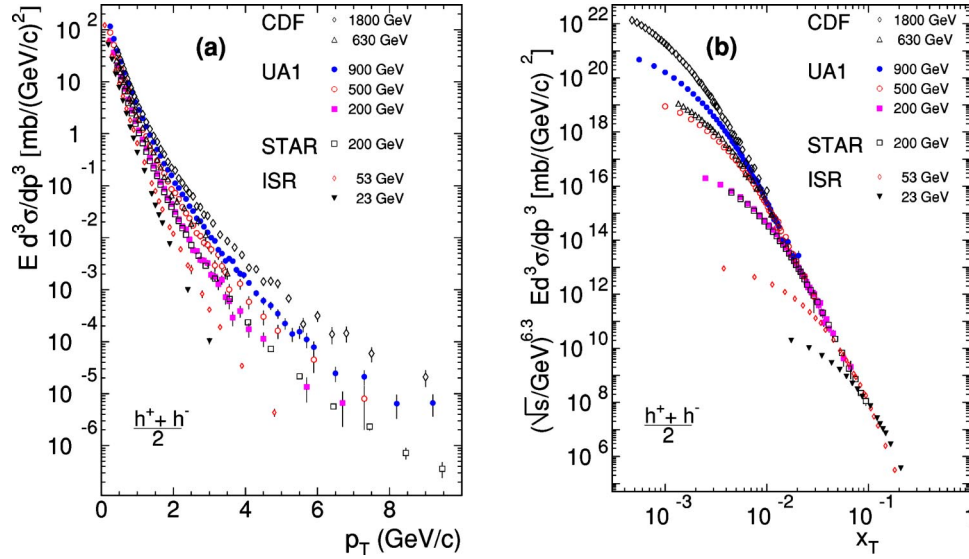


FIG. 15. (Color online) (a) Transverse momentum dependence of the invariant cross section at seven center-of-mass energies from different experiments [31,50,63,64]. (b) The same data multiplied by  $\sqrt{s}^{6.3}$ , plotted as a function of  $x_T = 2p_T/\sqrt{s}$ .

$$\sqrt{s}^{n(x_T, \sqrt{s})} \times E \frac{d^3\sigma}{dp^3} = G(x_T), \quad (20)$$

as a function of  $x_T$ , with  $n(x_T, \sqrt{s}) = 6.3$ . The  $(h^+ + h^-)/2$  data [Fig. 15(b)] show an asymptotic power law with increasing  $x_T$ . Data at a given  $\sqrt{s}$  fall below the asymptote at successively lower values of  $x_T$  with increasing  $\sqrt{s}$ , corresponding to the transition region from hard to soft physics in the  $p_T$  range of 1–2 GeV/c. The  $\pi^0$  data [Fig. 16(b)] show a similar  $x_T$  scaling but without the deviation at low  $x_T$ , since all available data are for  $p_T$  larger than 1–2 GeV/c. For larger  $x_T \geq 0.3$ , a value of  $n = 5.1$  [66,72] improves the scaling for the three lower c.m. energies,  $\sqrt{s} = 38.7, 52.7,$  and  $62.4$  GeV. It will be a challenge at

RHIC to obtain data in this  $x_T$  range to see whether the value of  $n \sim 5$  is the asymptotic limit for inclusive single particle production or whether  $n$  reaches the (LO) QCD value of 4.  $x_T$  scaling has also been studied in jet production at  $\sqrt{s} = 630$  and 1800 GeV [73], where  $n = 4.45$  is observed in the jet  $x_T$  range 0.15–0.3.

In Au+Au collisions,  $x_T$  scaling should work just as well as in  $p+p$  collisions and should yield the same value of  $n(x_T, \sqrt{s})$  if the high- $p_T$  particles are the result of hard scattering according to QCD. This is because the structure and fragmentation functions in Au+Au collisions should scale, so that Eq. (19) applies, albeit with a different  $G(x_T)$ . Thus, if the suppression of high- $p_T$  particles with respect to pointlike scaling from  $p+p$  collisions is due to shadowing of the structure functions [47] or gluon saturation [26], which are basi-

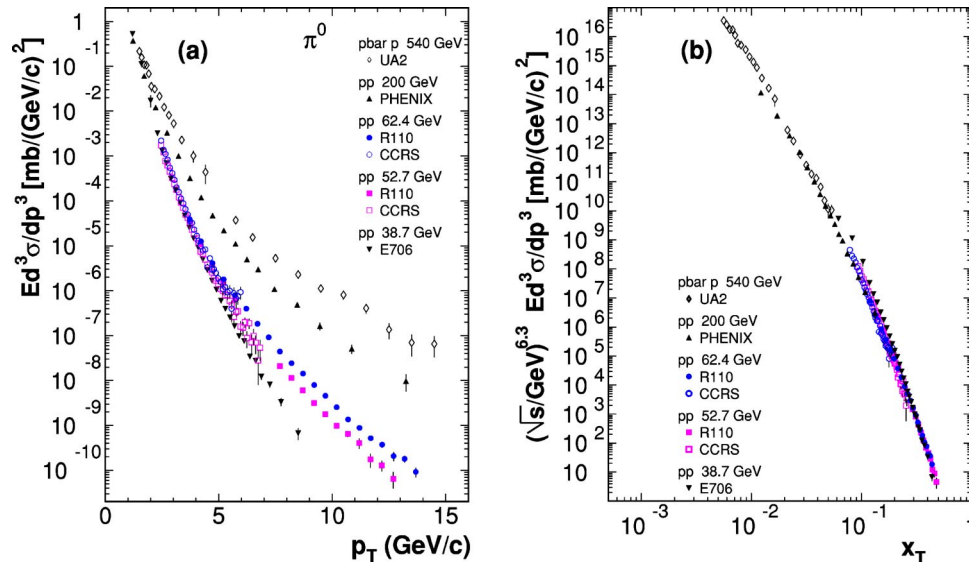


FIG. 16. (Color online) (a) Transverse momentum dependence of the invariant cross section for  $\pi^0$  at five center-of-mass energies from different experiments [16,65–68]. (b) The same data multiplied by  $\sqrt{s}^{6.3}$ , plotted vs  $x_T = 2p_T/\sqrt{s}$ .

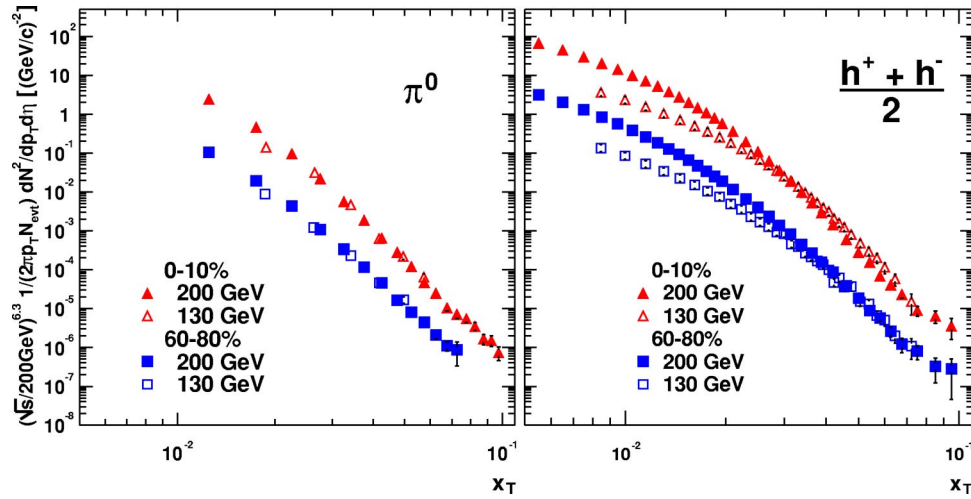


FIG. 17. (Color online)  $x_T$  scaled spectra for central collisions and peripheral collisions at  $\sqrt{s_{NN}}=130$  and 200 GeV. The left figure shows the  $\pi^0$   $x_T$  spectra, and the right figure shows the  $(h^+ + h^-)/2$   $x_T$  spectra. The central (0–10%)  $x_T$  spectra are represented by triangular symbols, and the peripheral (60–80%)  $x_T$  spectra are represented by square symbols. The open symbols represent  $x_T$  spectra from  $\sqrt{s_{NN}}=130$  GeV scaled by a factor of  $(130/200)^{6.3}$ . The solid symbols represent  $x_T$  spectra from  $\sqrt{s_{NN}}=200$  GeV. The error bars are statistical only.

cally scaling effects,<sup>4</sup> rather than due to a final state interaction with the dense medium, which may not scale, the cross sections [Eq. (19)] at a given  $x_T$  (and centrality) should all exhibit the same suppression. The initial state shadowing may cause  $G(x_T)$  to change with centrality, but  $n(x_T, \sqrt{s})$  should remain constant. In the case of the interaction with the dense medium,  $x_T$  scaling may or may not hold, depending on the details of the energy loss, for instance, whether or not the energy loss of the hard-scattered parton scales with its energy. It is also conceivable that the high- $p_T$  particles observed in Au+Au collisions at RHIC have nothing to do with QCD hard scattering [27,33,52]. In this case, striking differences from Eq. (19) and the systematics observed in  $p+p$  collisions should be expected.

To test  $x_T$  scaling in Au+Au collisions, we plot the quantities defined by Eq. (20) in Fig. 17 for charged hadron and  $\pi^0$  data from  $\sqrt{s_{NN}}=130$  GeV and 200 GeV for central (0–10%) and peripheral (60–80%) collisions. For the power  $n$ , we use the same value  $n(x_T, \sqrt{s})=6.3$  that was used for the  $p+p$  data shown in Fig. 15(b) and Fig. 16(b). The data are consistent with  $x_T$  scaling over the range  $0.03 \leq x_T \leq 0.06$  for  $\pi^0$  and  $0.04 \leq x_T \leq 0.075$  for  $(h^+ + h^-)/2$ .

According to Eq. (19), the ratio of inclusive cross sections at fixed  $x_T$  equals  $(200/130)^n$ . Thus, the power  $n(x_T, \sqrt{s})$  is related directly to the logarithm of the ratio of invariant hadron yield at fixed  $x_T$  as

$$n(x_T) = \frac{\log [\text{yield}(x_T, 130 \text{ GeV})/\text{yield}(x_T, 200 \text{ GeV})]}{\log(200/130)}. \quad (21)$$

The power  $n$ 's for both neutral pions and charged hadrons for central and peripheral collisions are shown in Fig. 18.

<sup>4</sup>There is a slight nonscaling effect of the structure functions [47] since for fixed  $x_T$ ,  $Q^2$  changes by a factor of 2.4 between the two  $\sqrt{s_{NN}}$ .

While the  $\pi^0$  data in central and peripheral collisions and charged hadron data in peripheral collisions seem to favor a similar power  $n$ , the charged hadron data from central collisions require a larger value of  $n$ .

For a more quantitative analysis, the Au+Au data for a given centrality and hadron selection are fitted simultaneously for  $\sqrt{s_{NN}}=130$  and 200 GeV to the form

$$\left(\frac{A}{\sqrt{s}}\right)^n (x_T)^{-m}, \quad (22)$$

where we have approximated Eq. (19) by using a constant power  $n(x_T, \sqrt{s})$  and a power law,  $x_T^{-m}$ , for  $G(x_T)$  over a limited range in  $x_T$ . The fit results and errors are quoted in Table VI. The corresponding ratios of yields are presented by lines in Figure 18, where the fit ranges ( $0.03 \leq x_T \leq 0.06$  for  $\pi^0$ s and  $0.04 \leq x_T \leq 0.074$  for charged hadrons) are indicated by the length of the line.

For peripheral collisions the fitted values for the power are  $n=6.33 \pm 0.54$  and  $n=6.12 \pm 0.49$ , for  $\pi^0$  and charged hadrons respectively, which are in quantitative agreement with the expectation from  $p+p$  collisions. Approximate  $x_T$  scaling in peripheral Au+Au collisions with the same power as observed in  $p+p$  collisions indicates that hard scattering is the dominating production mechanism for high- $p_T$  particles. In central collisions, neutral pions also exhibit  $x_T$  scaling with a similar power,  $n=6.41 \pm 0.55$ . Thus, it seems that high- $p_T$   $\pi^0$  production is consistent with hard scattering, with scaling structure and fragmentation functions, for all centralities.

For charged hadrons, the power found for central collisions is  $n=7.53 \pm 0.44$ . Most of the systematic errors are common and cancel between central and peripheral collisions, thus the difference of the two powers found for charged hadrons,  $\Delta n = n_{cent} - n_{periph} = 1.41 \pm 0.43$  compared with that for neutral pion  $\Delta n = 0.09 \pm 0.47$ , is significant.

This difference is consistent with the large proton and antiproton enhancement in central Au+Au collisions for in-

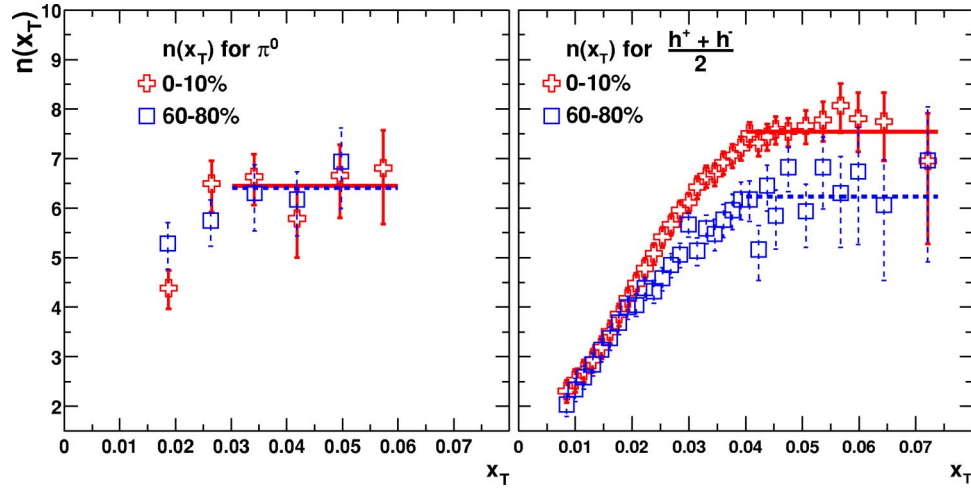


FIG. 18. (Color online) The  $x_T$  scaling power  $n$  [according to Eq. (21)] plotted as a function of  $x_T$  calculated for  $\pi^0$  (left) and  $(h^+ + h^-)/2$  (right) in central (0–10%) and peripheral (60–80%) collisions. The solid (and dashed) lines indicate a constant fit along with the fitting ranges to the central (and peripheral)  $n(x_T)$  functions. The error bars at each data point include statistical and point-to-point systematic errors from  $\sqrt{s_{NN}}=130$  and 200 GeV. The scale errors on  $x_T$  spectra are 20.7% (15.9%) for  $\pi^0$   $x_T$  spectra ratio in central (peripheral) collisions, and 18.6% (15.7%) for  $(h^+ + h^-)/2$   $x_T$  spectra ratio in central (peripheral) collisions. These type of errors propagate into the systematic errors on  $x_T$  scaling power  $n$  listed in Table VI.

intermediate  $p_T$  seen at  $\sqrt{s_{NN}}=130$  and 200 GeV, which appears to violate  $x_T$  scaling. The  $x_T$  range  $0.04 \leq x_T \leq 0.074$  corresponds to  $4 < p_T < 7.4$  GeV/c at  $\sqrt{s_{NN}}=200$  GeV, but it corresponds to  $2.6 < p_T < 4.8$  GeV/c at  $\sqrt{s_{NN}}=130$  GeV. If protons are enhanced at  $2 < p_T < 4.5$  GeV/c in central collisions at both  $\sqrt{s_{NN}}=130$  GeV and 200 GeV, then  $n_{cent}$  will be larger than  $n_{periph}$  in the measured  $x_T$  range. Since  $\sqrt{s_{NN}}=200$  GeV data indicate that the proton enhancement is limited to the medium  $p_T$  range, based on the equality of  $R_{AA}$  for charged hadrons and  $\pi^0$  at  $p_T > 4.5$  GeV/c (Fig. 12), this difference should go away at larger  $x_T$ .

#### IV. SUMMARY

We have presented a systematic study of the  $p_T$  and centrality dependence of charged hadron production at

$|\eta| < 0.18$  at  $\sqrt{s_{NN}}=200$  GeV. The yields per nucleon-nucleon collision in central collisions are significantly suppressed compared to peripheral and nucleon-nucleon collisions. The suppression is approximately independent of  $p_T$  above 4.5 GeV/c for all centrality classes, suggesting a similar spectral shape between Au+Au and  $p+p$  collisions. At  $p_T > 4.5$ , charged hadron suppression is the same as for neutral pions; the ratio  $h/\pi^0$  is  $\sim 1.6$  for all centralities, similar to the  $h/\pi$  value measured in  $p+p$  and  $e^+e^-$  collisions. The similar spectral shape and particle composition at high  $p_T$  are consistent with jet fragmentation as the dominating mechanism of particle production in Au+Au collisions for  $p_T > 4-5$  GeV/c. For both charged hadrons and neutral pions, the suppression sets in gradually from peripheral to central collisions, consistent with the expectation of partonic

TABLE VI. Results of the simultaneous fit to  $\sqrt{s_{NN}}=130$  and 200 GeV data using Eq. (22). The fit ranges are  $0.03 \leq x_T \leq 0.06$  for  $\pi^0$  and  $0.04 \leq x_T \leq 0.074$  for charged hadron. Only statistical and point-to-point systematic errors on the data points are included in the fit, which gives the statistical error on  $n$ . The normalization errors and other  $p_T$  correlated systematic errors are not included in the fit but are directly translated into a systematic error on  $n$ .

Fitting results for $\pi^0$ over $0.03 < x_T < 0.06$		
Parameters	0–10% centrality bin	60–80% centrality bin
$A$	$0.973 \pm 0.232$	$0.843 \pm 0.3$
$m$	$8.48 \pm 0.17$	$7.78 \pm 0.22$
$n$	$6.41 \pm 0.25(\text{stat})$ $\pm 0.49(\text{sys})$	$6.33 \pm 0.39(\text{stat})$ $\pm 0.37(\text{sys})$
Fitting results for $h^+ + h^-$ over $0.04 < x_T < 0.074$		
$A$	$2.30 \pm 0.44$	$0.62 \pm 0.27$
$m$	$8.74 \pm 0.28$	$8.40 \pm 0.43$
$n$	$7.53 \pm 0.18(\text{stat})$ $\pm 0.40(\text{sys})$	$6.12 \pm 0.33(\text{stat})$ $\pm 0.36(\text{sys})$

energy loss and surface emission of high- $p_T$  hadrons. The  $x_T$ -scaled hadron yields are compared between  $\sqrt{s_{NN}} = 130$  GeV and  $\sqrt{s_{NN}} = 200$  GeV Au+Au collisions. We find that the  $x_T$  scaling power  $n$  calculated for neutral pions in central and peripheral collisions and charged hadron in peripheral collisions is  $6.3 \pm 0.6$ , similar to  $p+p$  collisions. This again points towards similar production dynamics, i.e., hard scattering processes as described by QCD. However,  $n$  is  $7.5 \pm 0.5$  for charged hadrons in central collisions, indicating a strong nonscaling modification of particle composition of charged hadron spectra from that of  $p+p$  at intermediate  $p_T$ , 2–4.5 GeV/ $c$ . This is consistent with the large  $h/\pi^0$  ratios observed over the same  $p_T$  range in central collisions.

### ACKNOWLEDGMENTS

We thank the staff of the Collider-Accelerator and Physics Departments at Brookhaven National Laboratory and the staff of the other PHENIX participating institutions for their vital contributions. We acknowledge support from the Department of Energy, Office of Science, Nuclear Physics Division, the National Science Foundation, Abilene Christian University Research Council, Research Foundation of SUNY, and Dean of the College of Arts and Sciences,

Vanderbilt University (USA), Ministry of Education, Culture, Sports, Science, and Technology and the Japan Society for the Promotion of Science (Japan), Conselho Nacional de Desenvolvimento Científico e Tecnológico and Fundação de Amparo à Pesquisa do Estado de São Paulo (Brazil), Natural Science Foundation of China (People's Republic of China), Centre National de la Recherche Scientifique, Commissariat à l'Énergie Atomique, Institut National de Physique Nucléaire et de Physique des Particules and Institut National de Physique Nucléaire et de Physique des Particules, (France), Bundesministerium fuer Bildung und Forschung, Deutscher Akademischer Austausch Dienst, and Alexander von Humboldt Stiftung (Germany), Hungarian National Science Fund, OTKA (Hungary), Department of Atomic Energy and Department of Science and Technology (India), Israel Science Foundation (Israel), Korea Research Foundation and Center for High Energy Physics (Korea), Russian Ministry of Industry, Science and Tekhnologies, Russian Academy of Science, Russian Ministry of Atomic Energy (Russia), VR and the Wallenberg Foundation (Sweden), the U.S. Civilian Research and Development Foundation for the Independent States of the Former Soviet Union, the US-Hungarian NSF-OTKA-MTA, the US-Israel Binational Science Foundation, and the 5th European Union TMR Marie-Curie Programme.

- 
- [1] F. Karsch, Lect. Notes Phys. **583**, 209 (2002).
  - [2] L. McLerran, Lect. Notes Phys. **221**, 1 (1985); M. Gyulassy, Z. Phys. C **38**, 1 (1988).
  - [3] T. Alber *et al.*, NA49 Collaboration, Phys. Rev. Lett. **75**, 3814 (1995).
  - [4] K. Adcox *et al.*, PHENIX Collaboration, Phys. Rev. Lett. **87**, 052301 (2001).
  - [5] A. Bazilevsky *et al.*, PHENIX Collaboration, Nucl. Phys. **A715**, 486 (2003).
  - [6] J. D. Bjorken, Phys. Rev. D **27**, 140 (1983).
  - [7] D. Teaney *et al.*, Phys. Rev. Lett. **86**, 4783 (2001).
  - [8] U. Heinz and P. Kolb, Nucl. Phys. **A702**, 269 (2002).
  - [9] W. Broniowski and W. Florkowski, Phys. Rev. Lett. **87**, 272302 (2001); W. Florkowski and W. Broniowski, Phys. Rev. C **65**, 064905 (2002).
  - [10] M. Gyulassy and M. Plümer, Phys. Lett. B **243**, 432 (1990); X. N. Wang and M. Gyulassy, Phys. Rev. Lett. **68**, 1480 (1992); R. Baier *et al.*, Phys. Lett. B **345**, 277 (1995).
  - [11] R. Baier, D. Schiff, and B. G. Zakharov, Annu. Rev. Nucl. Part. Sci. **50**, 37 (2000).
  - [12] R. Baier, Y. L. Dokshitzer, A. H. Mueller, and D. Schiff, J. High Energy Phys. **9**, 33 (2001).
  - [13] X. N. Wang, Phys. Rev. C **63**, 054902 (2001).
  - [14] X. N. Wang, Nucl. Phys. **A715**, 775 (2003).
  - [15] J. F. Owens *et al.*, Phys. Rev. D **18**, 1501 (1978).
  - [16] S. S. Adler *et al.*, PHENIX Collaboration, Phys. Rev. Lett. **91**, 241803 (2003) and reference therein.
  - [17] K. Adcox *et al.*, PHENIX Collaboration, Phys. Rev. Lett. **88**, 022301 (2002).
  - [18] C. Adler *et al.*, STAR Collaboration, Phys. Rev. Lett. **89**, 202301 (2002).
  - [19] K. Adcox *et al.*, PHENIX Collaboration, Phys. Lett. B **561**, 82 (2003).
  - [20] B. B. Back *et al.*, PHOBOS Collaboration, nucl-ex/0302015.
  - [21] S. S. Adler *et al.*, PHENIX Collaboration, Phys. Rev. Lett. **91**, 072301 (2003).
  - [22] J. Adams *et al.*, STAR Collaboration, Phys. Rev. Lett. **91**, 172302 (2003).
  - [23] I. Arsene, *et al.*, BRAHMS Collaboration, Phys. Rev. Lett. **91**, 072305 (2003).
  - [24] M. Gyulassy, I. Vitev, and X. N. Wang, Phys. Rev. Lett. **86**, 2537 (2001).
  - [25] G. G. Barnafoldi, P. Levai, G. Papp, G. Fai, and Y. Zhang, nucl-th/0212111.
  - [26] D. Kharzeev, E. Levin, and L. McLerran, Phys. Lett. B **561**, 93 (2003), and references therein.
  - [27] K. Gallmeister, C. Greiner, and Z. Xu, nucl-th/0202051; K. Gallmeister, C. Greiner, and Z. Xu, Phys. Rev. C **67**, 044905 (2003).
  - [28] K. Adcox *et al.*, PHENIX Collaboration, Phys. Rev. Lett. **88**, 242301 (2002).
  - [29] S. S. Adler *et al.*, PHENIX Collaboration, Phys. Rev. Lett. **91**, 172301 (2003).
  - [30] J. Adams *et al.*, STAR Collaboration, nucl-ex/0306007.
  - [31] B. Alper *et al.*, Nucl. Phys. **B100**, 237 (1975).
  - [32] P. Abreu *et al.*, Eur. Phys. J. C **17**, 207 (2000); O. Klapp, Doctoral thesis, University Wuppertal, 1999.
  - [33] R. C. Hwa and C. B. Yang, Phys. Rev. C **67**, 034902 (2003); R. J. Fries, B. Muller, C. Nonaka, and S. A. Bass, Phys. Rev. Lett. **90**, 202303 (2003); V. Greco, C. M. Ko, and P. Levai, *ibid.* **90**, 202302 (2003); Phys. Rev. C **68**, 034904 (2003); R. J. Fries, B. Müller, C. Nonaka, and S. A. Bass, *ibid.* **68**,

- 044902 (2003).
- [34] K. Adcox *et al.*, Nucl. Instrum. Methods Phys. Res. A **499**, 469 (2003).
- [35] R. J. Glauber and G. Matthiae, Nucl. Phys. **B21**, 135 (1970).
- [36] Woods-Saxon Au nuclear radius  $R=6.38^{+0.27}_{-0.13}$  fm, diffusivity  $a=0.53\pm 0.01$  fm [B. Hahn, D. G. Ravenhall, and R. Hofstadter, Phys. Rev. **101**, 1131 (1956)], and nucleon-nucleon cross section  $\sigma_{NN}^{inel}=42\pm 3$  mb.
- [37] K. Adcox *et al.*, PHENIX Collaboration, Phys. Rev. Lett. **86**, 3500 (2001).
- [38] K. Adcox *et al.*, PHENIX Collaboration, nucl-ex/0307010.
- [39] K. Adcox *et al.*, Nucl. Instrum. Methods Phys. Res. A **499**, 489 (2003); J. T. Mitchell *et al.*, *ibid.* **482**, 491 (2002).
- [40] M. Aizawa *et al.*, Nucl. Instrum. Methods Phys. Res. A **499**, 508 (2003).
- [41] X. N. Wang and M. Gyulassy, Phys. Rev. D **44**, 3501 (1991).
- [42] K. Adcox *et al.*, PHENIX Collaboration, Phys. Rev. Lett. **89**, 092302 (2002).
- [43] C. Adler *et al.*, STAR Collaboration, nucl-ex/0206008.
- [44] GEANT 3.2.1, CERN program library.
- [45] S. S. Adler *et al.*, Nucl. Instrum. Methods Phys. Res. A **409**, 593 (2003).
- [46] S. S. Adler *et al.*, PHENIX Collaboration, nucl-ex/0307022.
- [47] K. J. Eskola, V. J. Kolhinen, and P. V. Ruuskanen, Nucl. Phys. **B535**, 351 (1998); K. J. Eskola, V. J. Kolhinen, and C. A. Salgado, Eur. Phys. J. C **9**, 61 (1999).
- [48] D. Antreasyan *et al.*, Phys. Rev. D **19**, 764 (1979).
- [49] T. Alexopoulos *et al.*, Phys. Rev. D **48**, 984 (1993).
- [50] C. Albajar *et al.*, Nucl. Phys. **B335**, 261 (1990).
- [51] I. Vitev and M. Gyulassy, Phys. Rev. Lett. **89**, 252301 (2002).
- [52] I. Vitev and M. Gyulassy, Phys. Rev. C **65**, 041902(R) (2002).
- [53] X. F. Zhang and G. Fai, hep-ph/0306227.
- [54] B. Müller, Phys. Rev. C **67**, 061901 (2003).
- [55] M. Breidenbach *et al.*, Phys. Rev. Lett. **23**, 935 (1969); see also W. K. H. Panofsky, in *Proceedings of the Fourteenth International Conference On High Energy Physics, Vienna, Austria, 1968* (CERN Scientific Information Service, Geneva, Switzerland, 1968), p. 23.
- [56] J. D. Bjorken, Phys. Rev. **179**, 1547 (1969).
- [57] S. M. Berman, J. D. Bjorken, and J. B. Kogut, Phys. Rev. D **4**, 3388 (1971).
- [58] R. Blankenbecler, S. J. Brodsky, and J. F. Gunion, Phys. Lett. **42B**, 461 (1972).
- [59] F. W. Büsser *et al.*, Phys. Lett. **46B**, 471 (1973); see also *Proceedings of the 16th International Conference of HEP*, edited by J. D. Jackson and A. Roberts (NAL, Batavia, IL, 1972), Vol. 3, p. 317.
- [60] M. Banner *et al.*, Phys. Lett. **44B**, 537 (1973).
- [61] B. Alper *et al.*, Phys. Lett. **44B**, 521 (1973).
- [62] R. F. Cahalan, K. A. Geer, J. Kogut, and L. Susskind Phys. Rev. D **11**, 1199 (1975).
- [63] F. Abe *et al.*, Phys. Rev. Lett. **61**, 1819 (1988).
- [64] J. Adams *et al.*, STAR Collaboration, Phys. Rev. Lett. **91**, 072304 (2003).
- [65] F. W. Büsser *et al.*, Nucl. Phys. **B106**, 1 (1976).
- [66] A. L.S. Angelis *et al.*, Phys. Lett. **79B**, 505 (1978); see also, A. G. Clark *et al.*, *ibid.* **74B**, 267 (1978).
- [67] M. Banner *et al.*, Phys. Lett. **115B**, 59 (1982); Z. Phys. C **27**, 329 (1985).
- [68] L. Apanasevich *et al.*, Phys. Rev. D **68**, 052001 (2003).
- [69] P. Darriulat, Annu. Rev. Nucl. Part. Sci. **30**, 159 (1980).
- [70] L. DiLella, Annu. Rev. Nucl. Part. Sci. **35**, 107 (1985).
- [71] J. F. Owens, Phys. Rev. D **11**, 1199 (1975); Rev. Mod. Phys. **59**, 465 (1987).
- [72] C. Kourkoumelis *et al.*, Phys. Lett. **84B**, 271 (1979).
- [73] J. Huston, in *Proceedings of the 29th International Conference of HEP (ICHEP 98), Vancouver, Canada, 1998*, edited by A. Astbury and J. Robinson (World Scientific, Singapore, 1999).